

# Channel Estimation in RIS-Assisted MIMO Systems Operating Under Imperfections

Paulo R. B. Gomes, Gilderlan T. de Araújo, Bruno Sokal, André L. F. de Almeida, *Senior Member, IEEE*, Behrooz Makki, *Senior Member, IEEE*, and Gábor Fodor, *Senior Member, IEEE*

**Abstract**—The promising gains of reconfigurable intelligent surface (RIS)-assisted multiple-input multiple-output (MIMO) systems, in terms of extended coverage and enhanced capacity, are critically dependent on the accuracy of the channel state information. However, traditional channel estimation (CE) schemes are not applicable in RIS-assisted MIMO networks since passive RISs typically lack the signal processing capabilities that are assumed by CE algorithms. This becomes problematic when physical imperfections or electronic impairments affect the RIS due to its exposition to different environmental effects or caused by hardware limitations from the circuitry. While these real-world effects are typically ignored in the literature, in this paper, we propose efficient CE schemes for RIS-assisted MIMO systems, taking different imperfections into account. Specifically, we propose two sets of tensor-based algorithms based on the parallel factor analysis decomposition schemes. First, assuming a long-term model – where the RIS imperfections, modeled as unknown phase shifts, are static within the channel coherence time – we formulate an iterative alternating least squares (ALS)-based algorithm for the joint estimation of the unknown phase deviations and the communication channels. Then, we develop the short-term imperfection model, which allows both amplitude and phase RIS imperfections to be non-static with respect to the channel coherence time. We propose two iterative ALS-based and closed-form higher-order singular value decomposition-based algorithms for jointly estimating the channels and the unknown impairments. We also investigate the computational complexity and the identifiability of the proposed algorithms and study the effect of various imperfections on the CE quality. Simulation results show the effectiveness of our proposed tensor-based algorithms in terms of estimation accuracy and computational complexity.

**Index Terms**—Channel estimation, hardware impairments, tensor modeling, MIMO systems, reconfigurable intelligent surface.

## I. INTRODUCTION

The steadily increasing demands for ubiquitous wireless services drive the efforts by the research and standardization communities to improve coverage, system capacity as well as the reliability and quality of a growing number of applications [1], [2]. The continuous growth of the number of mobile subscriptions, devices, and traffic increases the number of deployed infrastructure nodes, which makes capital and operational expenditures as well as energy consumption challenging for mobile network operators [3]. In this context, reconfigurable intelligent surface (RIS) has emerged as a potential technology for future wireless networks [4]–[6]. An RIS is a planar structure that contains several low-cost passive reflecting elements that independently manipulate the parameters of the impinging signal, such as amplitude, phase, frequency, and polarization, not requiring any RF chain

[7], [8]. In this sense, the passive control of the incident wave makes the RIS a power-efficient and low-complexity technology [9]–[12].

The benefits of the RIS are greatly dependent on the quality of the available channel state information (CSI). This is because CSI is required to jointly design the passive and active beamformings [13], [14]. Due to the passive nature of the RIS, channel estimation (CE) of the involved channels (i.e., gNB-RIS and RIS-user equipment (UE)) is not performed at the RIS but only on gNB or UE side. Recognizing this issue [15] proposes an ON/OFF method<sup>1</sup>, in which the cascaded channel (gNB-RIS-UE) is estimated. In this sense, [16] exploits compressed sensing (CS) and deep learning tools to reduce the training overhead. Reference [17] proposes a new signal modeling based on a proper vectorization and reduction operation for the channel estimation. Apart from pilot-assisted channel estimation, recently, reference [18] provides a solution to jointly estimate the symbols and recover the signal, which can imply a pilot overhead reduction.

In a realistic scenario, the RIS is subject to physical/hardware limitations or environmental impairments, e.g., water precipitations, snowflakes, sleet, dry/damp sand particles) [19]–[22]. A more realistic performance evaluation of RIS potential gains must take these issues into account. The presence of such nonidealities can be modeled as unwanted amplitude response attenuation and phase shift perturbations, leading to static or time-varying distortions in the received signal [23]–[27]. The presence of these impairments makes the channel estimation task even more challenging. The papers [19] and [20] propose channel estimation schemes that take into account RIS impairments in the context of single- and multi-user MIMO systems, respectively. However, these works do not capture/model the temporal variations of the RIS imperfections while considering a geometrical channel model. Differently from [19] and [20], we consider both short and long-term time-varying RIS impairments. Other works have investigated the effect of hardware impairments in RIS-assisted communications, such as [28] and [29]. The first investigates the beamforming design under hardware impairments, while the second concentrates on RIS diagnosis. However, these works do not consider the channel estimation problem.

Tensor algebra has been successfully applied to signal modeling and processing in wireless communications by exploiting the intrinsic multidimensional structure of wireless signals and

<sup>1</sup>It is worth mentioning that [15] considers a non-perfect ON/OFF reflection mode, which is of interesting practical aspect.

channels [30]–[32]. More recently, tensor-based approaches have been applied to the context of RIS-assisted wireless communications. The works [24] and [33] capitalize on the parallel factor (PARAFAC) decomposition to formulate an efficient iterative algorithm based on the ALS concept to solve the CE problem. Also, in [34] the authors develop a PARATUCK tensor model and semi-blind CE is carried out.

Tensor-based RIS-assisted channel estimation schemes allow the decoupling of the BS-RIS and RIS-UE channels while providing more flexible system parameter settings to be used for training [24]. In this paper, we enjoy the advantages of tensor modeling and tackle the joint channel and RIS imperfections estimation, by considering two relevant time-varying RIS impairments models. The main contribution of this paper can be summarized as follows.

- We propose tensor-based algorithms for the joint estimation of the involved channels and imperfections in RIS-assisted MIMO systems. We take both the long- and short-term imperfections into account. First, we show that the received signal under the long- and short-term imperfection models can be recast as tensors following trilinear and quadrilinear PARAFAC models, respectively.
- Exploiting the multi-linear structure of these models, we derive two sets of tensor-based algorithms. For the long-term imperfection (LTI) model, in which the RIS imperfections, modeled as unknown phase shifts, are static within channel coherence time, we formulate an iterative trilinear ALS-based algorithm called TALS-LTI for the joint estimation of the involved channels as well as the unknown RIS phase deviations.
- We generalize the imperfections behavior to be non-static with respect to the channel coherence time, referred to as the short-term imperfection (STI) model. For such a more challenging scenario, we propose iterative and closed-form tensor decomposition-based algorithms named TALS-STI and HOSVD-STI, respectively, to solve the joint channel and RIS imperfections estimation.
- We also study the identifiability of the proposed estimators, discuss their computational complexity and investigate the effect of imperfections on the network performance. The key features of the proposed tensor-based algorithms are their ability to properly estimate the channel and their robustness to different kinds of real-world imperfections at the RIS.

The simulation results show that, compared to the state-of-the-art methods, the proposed algorithms properly estimate the involved channels when different kinds of imperfections are taken into account. As an example, in the high signal-to-noise ratio (SNR) regime, our proposed algorithms improve the CE by approximately 100x compared to the method of [24], while present performance close to the lower-bound least squares (LS) estimator. Also, our proposed algorithms reduce considerably the overall computational complexity, compared to the related state-of-the-art method. Finally, the proposed TALS-LTI and TALS-STI algorithms are more flexible in the choices of training parameters compared to the proposed HOSVD-STI algorithm. Thus, the TALS-LTI and TALS-STI

algorithms are preferable when more flexible choices for training parameters are required, while the HOSVD-STI is preferred when a low processing delay is desired.

The rest of this paper is organized as follows. In Section II, the signal model of the RIS-assisted MIMO communication system operating under imperfections is introduced. We distinguish between two different types of imperfections under the RIS operation, namely, LTI and STI. Then, the CE problem is discussed for the LTI and STI scenarios. These signal models are reformulated as higher-order tensors following trilinear and quadrilinear PARAFAC models, from which two sets of iterative and closed-form tensor-based algorithms are developed for joint estimation of the involved channels and the RIS imperfections (Section III). A detailed identifiability analysis and its link to the system design recommendations as well as the computational complexity of the proposed tensor-based algorithms are provided in Section IV. Simulation results are presented in Section V. Finally, conclusions are drawn in Section VI.

*Notations and properties*<sup>2</sup>: The notation conventions and the properties that will be used throughout this paper are defined in the following. Scalars are denoted by lower-case letters ( $a$ ), column vectors by bold lower-case letters ( $\mathbf{a}$ ), matrices by bold upper-case letters ( $\mathbf{A}$ ) and tensors are represented by upper-case calligraphic letters ( $\mathcal{A}$ ). Then,  $\mathbf{A}^T$  and  $\mathbf{A}^\dagger$  stand for the transpose and Moore-Penrose pseudo-inverse of  $\mathbf{A}$ , respectively. The operator  $\text{vec}(\cdot)$  vectorizes its matrix argument by stacking its columns on top of each other, while  $\text{vecd}(\cdot)$  generates a vector out of the diagonal of its matrix argument. Also,  $\|\cdot\|_F$  is the Frobenius norm of a matrix or a tensor, which is defined as the square root of the sum of the squared of its elements.  $\lceil x \rceil$  is equal to the smallest integer that is greater than or equal to  $x$ . Moreover,  $\mathbf{I}_M$  is the  $M \times M$  identity matrix and  $j = \sqrt{-1}$  is the imaginary unit. The operator  $\mathbf{D}_i(\mathbf{A})$  generates a diagonal matrix from the  $i$ -th row of its matrix argument  $\mathbf{A}$ , while the operator  $\text{diag}(\mathbf{a})$  generates a diagonal matrix out of its vector argument  $\mathbf{a}$ . We define the Kronecker, Hadamard (element-wise product) and the outer product operators by  $\otimes$ ,  $\odot$  and  $\circ$ , respectively. The Khatri-Rao product (column-wise Kronecker product) between two matrices can be defined as

$$\mathbf{A} \diamond \mathbf{B} \doteq [\mathbf{D}_1(\mathbf{A})\mathbf{B}^T, \dots, \mathbf{D}_Q(\mathbf{A})\mathbf{B}^T]^T, \quad (1)$$

where  $\mathbf{A} = [\mathbf{a}_1, \dots, \mathbf{a}_Q] \in \mathbb{C}^{I \times Q}$  and  $\mathbf{B} = [\mathbf{b}_1, \dots, \mathbf{b}_Q] \in \mathbb{C}^{J \times Q}$ . Further, we shall make use of the following properties of the Khatri-Rao and Kronecker products

$$\text{vec}(\mathbf{A} \text{diag}(\mathbf{c}) \mathbf{B}^T) = (\mathbf{B} \diamond \mathbf{A}) \mathbf{c}, \forall \mathbf{A}, \mathbf{B}, \mathbf{c}, \quad (2)$$

$$\mathbf{a} \otimes \mathbf{b} \otimes \mathbf{c} = \text{vec}(\mathbf{c} \circ \mathbf{b} \circ \mathbf{a}), \forall \mathbf{a}, \mathbf{b}, \mathbf{c}. \quad (3)$$

## II. SIGNAL MODEL AND PROBLEM DESCRIPTION

In this section, we first introduce the signal model and describe in detail the two considered LTI and STI models.

<sup>2</sup>The definitions and operations involving tensors are in accordance with [35] and [36]. The  $n$ -mode unfolding matrix of  $\mathcal{A}$  along its  $n$ -th mode (or dimension) is represented by  $[\mathcal{A}]_{(n)}$ . The  $n$ -mode product between  $\mathcal{A}$  and  $\mathbf{B}$ , returns a tensor  $\mathcal{C} = \mathcal{A} \times_n \mathbf{B}$  such that  $[\mathcal{C}]_{(n)} = \mathbf{B} [\mathcal{A}]_{(n)}$ .

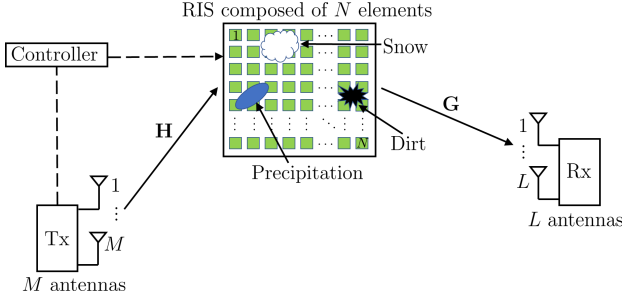


Fig. 1: An illustration of a RIS-assisted MIMO wireless communication system operating under imperfections.

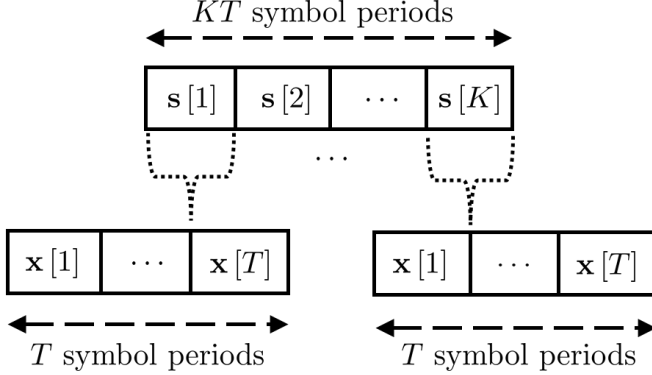


Fig. 2: An illustration of the considered CE protocol. The training time is divided into  $K$  time-blocks of duration  $T$  symbol periods each. The RIS activation pattern  $\mathbf{s}[k]$  is fixed during the  $k$ -th time-block and varies between different time-blocks while the pilot symbols  $\mathbf{x}[1], \dots, \mathbf{x}[T]$  are reused from block-to-block.

Our goal is to estimate the RIS-related channels and the RIS imperfection. As shown in Figure 1, we assume that the direct Tx-Rx link is too weak or unavailable, the focus being on the RIS-assisted link. Note, however, that if the Tx-Rx link is available, the direct channel can be estimated separately via any state-of-the-art MIMO channel estimation method.

#### A. RIS Operating under LTI

We consider a single-user narrowband RIS-assisted MIMO communication system, in which the transmitter (Tx) and the receiver (Rx) have arrays composed of  $M$  and  $L$  antennas, respectively. Without loss of generality, although this work assumes a downlink communication, our signal models also apply to the uplink communications by inverting the roles of the Tx and the Rx. To improve the communication performance, an RIS with  $N$  individually adjustable passive reflecting elements is deployed in a proper place that creates an alternative Tx-RIS-Rx link. The direct Tx-Rx link is assumed to be too weak or unavailable due to unfavorable propagation conditions. We also assume a block-fading channel where the Tx-RIS and RIS-Rx channels remain constant for at least  $k = 1, \dots, K$ , time-blocks, each with duration of  $T$  symbols, representing a total duration of  $KT$  symbol periods dedicated for CE within the channel coherence time.

Let us define the RIS activation pattern  $\mathbf{s}[k] \in \mathbb{C}^{N \times 1}$

configured at the  $k$ -th time-block as

$$\mathbf{s}[k] = [\beta_{1,k}e^{j\phi_{1,k}}, \dots, \beta_{N,k}e^{j\phi_{N,k}}]^T \in \mathbb{C}^{N \times 1}, \quad (4)$$

where  $0 \leq \phi_{n,k} \leq 2\pi$  and  $0 \leq \beta_{n,k} \leq 1$  denote the phase shift and the amplitude reflection coefficient of the  $n$ -th RIS element tuned at the  $k$ -th time-block  $\forall n = 1, \dots, N$ , and  $\forall k = 1, \dots, K$ , respectively. As a protocol for CE we assume the following (see Fig. 2):

- 1) At each time-block  $k = 1, \dots, K$ , of duration  $T$ , the elements of  $\mathbf{s}[k]$  are dynamically tuned in a passive way via the smart controller;
- 2) The activation pattern  $\mathbf{s}[k]$  remains constant within the  $k$ -th time-block but may vary between different time-blocks, yielding a total of  $\mathbf{s}[1], \dots, \mathbf{s}[K]$  different adjustable patterns to the RIS during the CE stage;
- 3) The pilot symbol  $\mathbf{x}[t, k] \in \mathbb{C}^{M \times 1}$  transmitted at the  $t$ -th symbol period within the  $k$ -th time-block is reused for each  $k = 1, \dots, K$ , i.e.,  $\mathbf{x}[t, k] = \mathbf{x}[t] \forall k = 1, \dots, K$ .

The baseband received pilot signal  $\mathbf{y}[t, k] \in \mathbb{C}^{L \times 1}$  associated with the  $t$ -th symbol period at the  $k$ -th time-block is given by

$$\mathbf{y}[t, k] = \mathbf{G} \text{diag}(\mathbf{s}[k]) \mathbf{H}^T \mathbf{x}[t] + \mathbf{v}[t, k]. \quad (5)$$

Collecting the received signals during the  $T$  symbol periods at the  $k$ -th time-block, the model in (5) can be rewritten as

$$\mathbf{Y}[k] = \mathbf{G} \text{diag}(\mathbf{s}[k]) \mathbf{H}^T \mathbf{X} + \mathbf{V}[k] \in \mathbb{C}^{L \times T}, \quad (6)$$

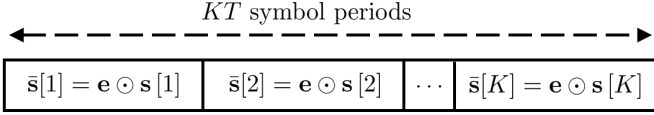
where  $\mathbf{Y}[k] = [\mathbf{y}[1, k], \dots, \mathbf{y}[T, k]] \in \mathbb{C}^{L \times T}$ . The matrices  $\mathbf{H} \in \mathbb{C}^{M \times N}$  and  $\mathbf{G} \in \mathbb{C}^{L \times N}$  are the Tx-RIS and RIS-Rx channels, respectively, while  $\mathbf{X} = [\mathbf{x}[1], \dots, \mathbf{x}[T]] \in \mathbb{C}^{M \times T}$  collects the pilot signals transmitted within the  $k$ -th time-block, and  $\mathbf{V}[k] = [\mathbf{v}[1, k], \dots, \mathbf{v}[T, k]] \in \mathbb{C}^{L \times T}$  is the additive white Gaussian noise (AWGN) matrix with zero mean and unit variance elements. In order to simplify our formulation and analysis, without loss of generality, we assume the transmission of the pilot signal  $\mathbf{X} = \mathbf{I}_M$ .

In this work, a special attention is given to the structure of the RIS activation pattern. In practice, some imperfections at the RIS elements are common to occur. Initially, we assume the case in which such imperfections induce long-term static phase shift perturbations at the RIS response. Such imperfections may come from, e.g., phase noise due to the finite resolution of the phase shifts or by phase estimation errors from imperfect CE. In the presence of these imperfections, the structure of the RIS activation pattern is modified in an undesired manner leading to the following resulting RIS reflection pattern that incorporates the imperfection contributions:

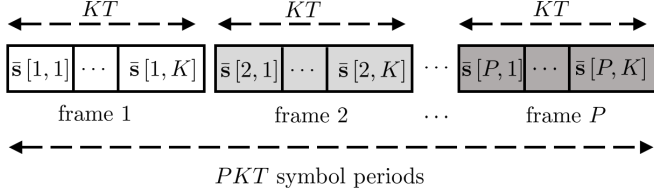
$$\begin{aligned} \bar{\mathbf{s}}[k] &= [\beta_{1,k}e^{j(\phi_{1,k}+\theta_1)}, \dots, \beta_{N,k}e^{j(\phi_{N,k}+\theta_N)}]^T \\ &= \mathbf{e} \odot \mathbf{s}[k] \in \mathbb{C}^{N \times 1}. \end{aligned} \quad (7)$$

Here,  $0 \leq \theta_n \leq 2\pi \forall n = 1, \dots, N$  denotes the phase shift perturbation that affects the  $n$ -th RIS element. where the entries of the random vector  $\mathbf{e} \in \mathbb{C}^{N \times 1}$  that collects all unknown existing phase perturbations are defined as

$$e_n = \begin{cases} 1, & \text{non-impaired case} \\ e^{j\theta_n}, & \text{otherwise,} \end{cases} \quad (8)$$



(a) An illustration of the LTI model. The vector  $\mathbf{e}$  with phase perturbations is static during the  $KT$  symbol periods.



(b) An illustration of the generalized STI model with time-varying RIS fluctuations during the channel coherence time.

Fig. 3: Illustration of the LTI and STI models considered in the paper.

for  $n = 1, \dots, N$ . Making use of definitions in (7) and (8), the impaired version of the received signal at the Rx node in (6) can be expressed as

$$\mathbf{Y}[k] = \mathbf{G} \text{diag} \left( \underbrace{\mathbf{e} \odot \mathbf{s}[k]}_{\bar{\mathbf{s}}[k]} \right) \mathbf{H}^T + \mathbf{V}[k] \in \mathbb{C}^{L \times M}, \quad (9)$$

$\forall k = 1, \dots, K$ . Equivalently, in matrix form we have

$$\mathbf{Y}[k] = \mathbf{G} \text{diag}(\mathbf{e}) \mathbf{D}_k(\mathbf{S}) \mathbf{H}^T + \mathbf{V}[k], \quad (10)$$

where  $\mathbf{S} = [\mathbf{s}[1], \dots, \mathbf{s}[K]]^T \in \mathbb{C}^{K \times N}$  collects in its rows the RIS activation patterns used across  $K$  time-blocks specifically configured for the CE.

Particularly, the impaired received signal in (10) considers an RIS operating under LTI that induces phase shift perturbations in the reflected signals. In other words, in this model we assume that the vector  $\mathbf{e} \in \mathbb{C}^{N \times 1}$  is formed only by phase components that remain static within the  $KT$  symbol periods. Figure 3a illustrates the considered LTI model. This occurs, for instance, when the behavior of the imperfections at the RIS elements are static compared to the channel coherence time.

### B. RIS Operating under STI

Here, we assume that the CE occurs after the receiver collects  $p = 1, \dots, P$ , frames composed of  $KT$  symbol periods each. The division of the reception time into  $P$  frames is motivated by possible short-term variations caused by the RIS imperfections, i.e., the imperfections changing more frequently. In this approach, the behavior of the imperfections induces both amplitude and phase perturbations in the RIS elements and have a non-static nature with respect to channel coherence time but they present stationary characteristics within each frame. Figure 3b illustrates the considered STI model. In contrast to the received signal model formulated in (10), this assumption implies that such imperfection model takes into account rapid amplitude and phase fluctuations at the RIS elements during the channel coherence time. Note that the STI induces a block-fading effect in the signals reflected by

the RIS during the  $PKT$  symbol periods for CE. Therefore, by considering a RIS operating under this STI model the resulting reflection pattern related to the  $k$ -th time-block at the  $p$ -th frame can be written as

$$\begin{aligned} \bar{\mathbf{s}}[p, k] &= [e_{1,p} \beta_{1,k} e^{j\phi_{1,k}}, \dots, e_{N,p} \beta_{N,k} e^{j\phi_{N,k}}]^T \\ &= \mathbf{e}[p] \odot \mathbf{s}[k] \mathbb{C}^{N \times 1}, \end{aligned} \quad (11)$$

where  $\mathbf{e}[p] = [e_{1,p}, \dots, e_{N,p}]^T \in \mathbb{C}^{N \times 1} \forall p = 1, \dots, P$ , depends on the  $p$ -th received frame and models the unknown non-static amplitude and phase fluctuations along the training time. The entries of the random vector  $\mathbf{e}[p]$  associated with the  $p$ -th frame are defined as

$$e_{n,p} = \begin{cases} 1, & \text{non-impaired case} \\ \alpha_{n,p} \cdot e^{j\theta_{n,p}}, & \text{otherwise,} \end{cases} \quad (12)$$

where  $0 \leq \alpha_{n,p} \leq 1$  and  $0 \leq \theta_{n,p} \leq 2\pi \forall n = 1, \dots, N$ , and  $\forall p = 1, \dots, P$ , denote the unwanted amplitude attenuation and phase shift perturbations that affect the  $n$ -th RIS element at the  $p$ -th frame, respectively. It is important to note that the model in (12) captures different kinds of real-world imperfections at the RIS. For example, we can note the follow situations:

- 1)  $\alpha_{n,p} \neq 0$  and  $\theta_{n,p} \neq 0$  represent the amplitude absorption and phase shift caused by an object suspended on the  $n$ -th RIS element [19], or caused by hardware impairments in the electronic circuits that make up the RIS [37].
- 2)  $\alpha_{n,p} = 1$  and  $\theta_{n,p} \neq 0$  represent the phase noise perturbations from low-resolution phase shifts or phase errors from imperfect CE [23]- [27].
- 3)  $\alpha_{n,p} = 0$  represents the maximum absorption i.e., the  $n$ -th RIS element is completely blocked [19].
- 4)  $\alpha_{n,p} = 1$  and  $\theta_{n,p} = 0$  represents the non-impaired RIS in which no imperfection affects its  $n$ -th element. Note that in this ideal case  $\bar{\mathbf{s}}[p, k] = \mathbf{s}[p, k]$  holds since  $e_{n,p} = 1 \forall n = 1, \dots, N$ , and  $\forall p = 1, \dots, P$ .

We also observe that the LTI model presented in Section II-A is a particular case of the generalized STI model when  $\alpha_{n,p} = 1$  for  $P = 1$  and  $n = 1, \dots, N$ . However, we study these two cases separately for a clearer description of the static and non-static imperfection scenarios.

By considering an RIS operating under the STI model, we can rewrite the received signal in (9) as

$$\mathbf{Y}[p, k] = \mathbf{G} \text{diag} \left( \underbrace{\mathbf{e}[p] \odot \mathbf{s}[k]}_{\bar{\mathbf{s}}[p, k]} \right) \mathbf{H}^T + \mathbf{V}[p, k], \quad (13)$$

$\forall p = 1, \dots, P$ , and  $\forall k = 1, \dots, K$ . In a more convenient form for our formulation, the received signal (13) can be written in its complete matrix and decoupled format as

$$\mathbf{Y}[p, k] = \mathbf{G} \mathbf{D}_p(\mathbf{E}) \mathbf{D}_k(\mathbf{S}) \mathbf{H}^T + \mathbf{V}[p, k], \quad (14)$$

where each row of the matrix  $\mathbf{E} = [\mathbf{e}[1], \dots, \mathbf{e}[P]]^T \in \mathbb{C}^{P \times N}$  collects the amplitude and phase parameters for the RIS elements impaired at the  $p$ -th frame. Throughout this work, for the two approaches formulated in Sections II-A and II-B, we assume that a number of  $N_B = NR_B$  random elements at the RIS are subject to imperfections, where  $R_B \in [0, 1]$  denotes its occurrence probability.

### C. Problem Description

In (7) and (11), the RIS reflection pattern corrupted with errors  $\bar{s}[k]$  and  $\bar{s}[p, k]$  induce unwanted amplitude and/or phase shift responses in the reflected signal by the RIS creating a mismatch between the ideal reflection pattern and the one that is actually applied by the RIS. To deal with these imperfections, in this work, we propose to jointly estimate the involved channels  $\mathbf{G}$  and  $\mathbf{H}$ , as well as the unknown imperfections that affect the  $N_B$  impaired elements at the RIS. Decoupled estimations of the channels are required, for instance, to optimize the phase shifts at the RIS, the transmit precoder at the transmitter and the receive combiner at the receiver in order to maximize the rate and energy efficiencies in the data transmission phase [13], [38]. However, the issues of how to utilize the estimated channels to jointly optimize the RIS phase shifts, the transmitter and receiver active beamformers, as well as the control overhead problem of optimal phase shifts [39], [40] are out of the scope of this work and will be addressed in future work.

In the following, we show that the received signal models in (10) and (14) can be represented as third- and fourth-order tensor models, respectively. Then, we show how such higher-order representations serve as reference models for the development of efficient PARAFAC-based algorithms to solve the CE problem for more realistic scenarios where the RIS operates under LTI and STI.

*Remark 1:* One could also consider discrete (quantized) phase shifts for the RIS. As shown in [41], [42], quantization errors due to finite phase shift resolution do not significantly affect the overall system performance and can be easily incorporated into the hardware impairment vector  $\mathbf{e}$  as an additional phase shift noise perturbation term. Hence, the proposed algorithms can also be applied to the quantized phase shift case.

## III. PROPOSED CE ALGORITHMS

In this section, we propose three different CE algorithms for the cases with LTI and STI.

### A. TALS Algorithm for RIS Operating under LTI (TALS-LTI)

We initially consider the scenario with  $N_B$  unknown passive elements of the RIS being affected by LTI as presented in Section II-A. The values of the phase perturbations as well as their positions are assumed to be unknown at the receiver.

For simplicity of presentation and without loss of generality, we neglect the noise term in our formulations. The noiseless part of the received signal in (10) can be identified as the  $k$ -th frontal slice of a third-order tensor  $\mathcal{Y} \in \mathbb{C}^{L \times M \times K}$  that follows the following PARAFAC decomposition [35]

$$\mathcal{Y} = \mathcal{I}_{3,N} \times_1 \mathbf{G} \times_2 \mathbf{H} \times_3 \bar{\mathbf{S}}. \quad (15)$$

Here,  $\mathcal{I}_{3,N}$  represents a third-order identity tensor of size  $N \times N \times N$ . According to (15), the factor matrices related to 1-mode, 2-mode and 3-mode of  $\mathcal{Y}$  are respectively  $\mathbf{G} \in \mathbb{C}^{L \times N}$ ,  $\mathbf{H} \in \mathbb{C}^{M \times N}$  and  $\bar{\mathbf{S}} = [\bar{s}[1], \dots, \bar{s}[K]]^T \in \mathbb{C}^{K \times N}$ , where  $\bar{s}[k] = \mathbf{e} \odot \mathbf{s}[k]$  or, equivalently, in matrix notation  $\mathbf{D}_k(\bar{\mathbf{S}}) = \text{diag}(\mathbf{e}) \mathbf{D}_k(\mathbf{S})$ ,  $\forall k = 1, \dots, K$ .

Resorting to the multilinear structure of the PARAFAC decomposition in (15), higher degrees of freedom for signal processing can be achieved by exploiting the dimensions of interest of the received signal tensor. In this sense,  $\mathcal{Y}$  can also be expressed with respect to its 1-mode and 2-mode unfoldings, which can be expressed as

$$\begin{aligned} [\mathcal{Y}]_{(1)} &= \mathbf{G} \text{diag}(\mathbf{e}) (\mathbf{S} \diamond \mathbf{H})^T \in \mathbb{C}^{L \times MK}, \quad \text{and} \\ [\mathcal{Y}]_{(2)} &= \mathbf{H} \text{diag}(\mathbf{e}) (\mathbf{S} \diamond \mathbf{G})^T \in \mathbb{C}^{M \times LK}, \end{aligned} \quad (16)$$

where  $[\mathcal{Y}]_{(1)} \in \mathbb{C}^{L \times MK}$  and  $[\mathcal{Y}]_{(2)} \in \mathbb{C}^{M \times LK}$  are obtained from (10) by stacking the frontal slices into wide matrices, as defined by

$$\begin{aligned} [\mathcal{Y}]_{(1)} &= [\mathbf{Y}[1], \dots, \mathbf{Y}[K]], \quad \text{and} \\ [\mathcal{Y}]_{(2)} &= [\mathbf{Y}^T[1], \dots, \mathbf{Y}^T[K]]. \end{aligned} \quad (17)$$

Additionally,  $[\mathcal{Y}]_{(1)}$  can also be represented in a convenient vectorized form. By applying the property (2) to  $[\mathcal{Y}]_{(1)}$  we obtain

$$\text{vec}([\mathcal{Y}]_{(1)}) = (\mathbf{S} \diamond \mathbf{H} \diamond \mathbf{G}) \mathbf{e} \in \mathbb{C}^{LMK \times 1}. \quad (18)$$

In the following, we describe an iterative way to estimate  $\mathbf{H}$  and  $\mathbf{G}$  for the RIS-assisted MIMO system with RIS operating under LTI. Let us define  $\tilde{\mathcal{Y}} = \mathcal{Y} + \mathcal{V}$  as the noisy version of the received signal tensor  $\mathcal{Y}$ , where  $\mathcal{V}$  denotes the additive noise tensor, the entries of which are modeled as zero-mean unit variance complex Gaussian random variables. The estimation problem can be formulated as follows

$$\min_{\mathbf{G}, \mathbf{H}, \mathbf{e}} \left\| \tilde{\mathcal{Y}} - \mathcal{I}_{3,N} \times_1 \mathbf{G} \times_2 \mathbf{H} \times_3 \bar{\mathbf{S}} \right\|_{\text{F}}^2. \quad (19)$$

This problem can be solved efficiently by means of the ALS algorithm [35], [43], which is a well-known iterative method for estimating the factor matrices of a tensor model thanks to its implementation simplicity and monotonic convergence property in which the update of every given matrix at each iteration may either improve or maintain but cannot worsen the current fit, leading usually to global minimum solution [44], [45]. The decoupled estimates of  $\mathbf{G}$ ,  $\mathbf{H}$  and  $\mathbf{e}$  can be obtained by converting the trilinear fitting problem in (19) into the following three simplest linear LS sub-problems formulated from (16) and (18), respectively

$$\hat{\mathbf{G}} = \underset{\mathbf{G} | \mathbf{e}, \mathbf{H}}{\text{argmin}} \left\| [\tilde{\mathcal{Y}}]_{(1)} - \mathbf{G} \text{diag}(\mathbf{e}) (\mathbf{S} \diamond \mathbf{H})^T \right\|_{\text{F}}^2, \quad (20)$$

$$\hat{\mathbf{H}} = \underset{\mathbf{H} | \mathbf{e}, \mathbf{G}}{\text{argmin}} \left\| [\tilde{\mathcal{Y}}]_{(2)} - \mathbf{H} \text{diag}(\mathbf{e}) (\mathbf{S} \diamond \mathbf{G})^T \right\|_{\text{F}}^2, \quad (21)$$

$$\hat{\mathbf{e}} = \underset{\mathbf{e} | \mathbf{H}, \mathbf{G}}{\text{argmin}} \left\| \text{vec}([\tilde{\mathcal{Y}}]_{(3)}) - (\mathbf{S} \diamond \mathbf{H} \diamond \mathbf{G}) \mathbf{e} \right\|_{\text{F}}^2. \quad (22)$$

According to (20), the conditional LS update for  $\hat{\mathbf{G}}$  is given by

$$\hat{\mathbf{G}} = [\tilde{\mathcal{Y}}]_{(1)} \left[ \text{diag}(\mathbf{e}) (\mathbf{S} \diamond \mathbf{H})^T \right]^\dagger. \quad (23)$$

Similarly, according to (21) and (22), the conditional LS updates for  $\hat{\mathbf{H}}$  and  $\hat{\mathbf{e}}$  are respectively given by

$$\hat{\mathbf{H}} = [\tilde{\mathcal{Y}}]_{(2)} \left[ \text{diag}(\mathbf{e}) (\mathbf{S} \diamond \mathbf{G})^T \right]^\dagger, \quad (24)$$

$$\hat{\mathbf{e}} = (\mathbf{S} \diamond \mathbf{H} \diamond \mathbf{G})^\dagger \text{vec}([\tilde{\mathcal{Y}}]_{(3)}). \quad (25)$$

---

**Algorithm 1: TALS-LTI Algorithm**


---

1. Set  $i = 0$ ;  
Keep  $\mathbf{S}$  fixed; Initialize randomly the matrix  $\hat{\mathbf{H}}_{(i=0)}$  and the imperfections vector  $\hat{\mathbf{e}}_{(i=0)}$ ;
  2.  $i \leftarrow i + 1$ ;
  3. Using (23), obtain an LS estimate of  $\hat{\mathbf{G}}_{(i)}$ :  
$$\hat{\mathbf{G}}_{(i)} = [\tilde{\mathcal{Y}}]_{(1)} \left[ \text{diag}(\hat{\mathbf{e}}_{(i-1)}) \left( \mathbf{S} \diamond \hat{\mathbf{H}}_{(i-1)} \right)^{\top} \right]^{\dagger};$$
  4. Using (24), obtain an LS estimate of  $\hat{\mathbf{H}}_{(i)}$ :  
$$\hat{\mathbf{H}}_{(i)} = [\tilde{\mathcal{Y}}]_{(2)} \left[ \text{diag}(\hat{\mathbf{e}}_{(i-1)}) \left( \mathbf{S} \diamond \hat{\mathbf{G}}_{(i)} \right)^{\top} \right]^{\dagger};$$
  5. Using (25), obtain an LS estimate of  $\hat{\mathbf{e}}_{(i)}$ :  
$$\hat{\mathbf{e}}_{(i)} = \left( \mathbf{S} \diamond \hat{\mathbf{H}}_{(i)} \diamond \hat{\mathbf{G}}_{(i)} \right)^{\dagger} \text{vec}([\tilde{\mathcal{Y}}]_{(3)});$$
  6. Compute the error  $\epsilon_{(i)} = \left\| [\tilde{\mathcal{Y}}]_{(1)} - [\hat{\mathcal{Y}}]_{(1)(i)} \right\|_{\text{F}}^2$   
where  $[\hat{\mathcal{Y}}]_{(1)(i)} = \hat{\mathbf{G}}_{(i)} \text{diag}(\hat{\mathbf{e}}_{(i)}) \left( \mathbf{S} \diamond \hat{\mathbf{H}}_{(i)} \right)^{\top}$ ;
  7. Repeat Steps 2-6 until  $|\epsilon_{(i)} - \epsilon_{(i-1)}| \leq \delta$ .
- 

The proposed TALS-STI algorithm consists of three iterative and alternating update steps formulated from the LS solutions in (23), (24) and (25). At each step, the fitting error is minimized with respect to one given factor matrix by fixing the other matrices to their values obtained at previous updating steps. This procedure is repeated until the convergence of the algorithm at the  $i$ -th iteration determined by the designer. Let define

$$[\hat{\mathcal{Y}}]_{(1)(i)} = \hat{\mathbf{G}}_{(i)} \text{diag}(\hat{\mathbf{e}}_{(i)}) \left( \mathbf{S} \diamond \hat{\mathbf{H}}_{(i)} \right)^{\top} \in \mathbb{C}^{L \times MK}, \quad (26)$$

as the reconstructed tensor obtained from the estimates of  $\hat{\mathbf{G}}_{(i)}$ ,  $\hat{\mathbf{H}}_{(i)}$ , and  $\hat{\mathbf{e}}_{(i)}$ , and the residual error as  $\epsilon_{(i)} = \left\| [\tilde{\mathcal{Y}}]_{(1)} - [\hat{\mathcal{Y}}]_{(1)(i)} \right\|_{\text{F}}^2$ , computed at the end of the  $i$ -th iteration. The convergence of the algorithm is declared when  $|\epsilon_{(i)} - \epsilon_{(i-1)}| \leq \delta$ , with  $\delta$  being a constant considered by the designer, meaning that the reconstruction error does not significantly change between two successive iterations. In this work, we set  $\delta = 10^{-6}$  as a convergence threshold. The implementation steps of the proposed iterative TALS-LTI algorithm are summarized in the pseudocode shown in Algorithm 1. For the complexity analysis of Algorithm 1, see Section IV.

### B. TALS Algorithm for RIS under STI (TALS-STI)

In order to derive proposed channel estimators for a scenario with STI, let us first establish a link between the received signal in (14) and the PARAFAC decomposition. According to [35], the noiseless signal part of (14) expresses the  $(p, k)$ -th frontal slice of a fourth-order tensor  $\mathcal{Y} \in \mathbb{C}^{L \times M \times K \times P}$  that follows the PARAFAC decomposition

$$\mathcal{Y} = \mathcal{I}_{4,N} \times_1 \mathbf{G} \times_2 \mathbf{H} \times_3 \mathbf{S} \times_4 \mathbf{E}. \quad (27)$$

Here,  $\mathcal{I}_{4,N}$  denotes the fourth-order identity tensor of size  $N \times N \times N \times N$ , while  $\mathbf{G}$ ,  $\mathbf{H}$ ,  $\mathbf{S}$  and  $\mathbf{E}$  are the 1,2,3,4-mode factor matrices of the decomposition, respectively.

By stacking column-wise the noiseless received signal in (14) for the  $K$  time-blocks at frame  $p$  as the matrix  $\mathbf{Y}_p = [\mathbf{Y}[p, 1], \dots, \mathbf{Y}[p, K]] \in \mathbb{C}^{L \times MK}$ , we have

$$\mathbf{Y}_p = \mathbf{G} \mathbf{D}_p(\mathbf{E}) [\mathbf{D}_1(\mathbf{S}) \mathbf{H}^{\top}, \dots, \mathbf{D}_K(\mathbf{S}) \mathbf{H}^{\top}], \quad (28)$$

$\forall p = 1, \dots, P$ . Applying the property (1) to the right-hand side of (28), a more compact form is obtained as

$$\mathbf{Y}_p = \mathbf{G} \mathbf{D}_p(\mathbf{E}) (\mathbf{S} \diamond \mathbf{H})^{\top} \in \mathbb{C}^{L \times MK}. \quad (29)$$

From (29), we can define the new column-wise collection  $[\mathcal{Y}]_{(1)} = [\mathbf{Y}_1, \dots, \mathbf{Y}_P] \in \mathbb{C}^{L \times MKP}$  as the 1-mode matrix unfolding of the received signal tensor  $\mathcal{Y} \in \mathbb{C}^{L \times M \times K \times P}$  in (27), which is given by

$$[\mathcal{Y}]_{(1)} = \mathbf{G} \left[ \mathbf{D}_1(\mathbf{E}) (\mathbf{S} \diamond \mathbf{H})^{\top}, \dots, \mathbf{D}_P(\mathbf{E}) (\mathbf{S} \diamond \mathbf{H})^{\top} \right]. \quad (30)$$

By applying property (1) to the right-hand side of (30), we finally obtain

$$[\mathcal{Y}]_{(1)} = \mathbf{G} (\mathbf{E} \diamond \mathbf{S} \diamond \mathbf{H})^{\top} \in \mathbb{C}^{L \times MKP}. \quad (31)$$

Additionally, for our purpose, we also need to define the 2-mode, 3-mode and 4-mode matrix unfoldings of the fourth-order received signal tensor  $\mathcal{Y} \in \mathbb{C}^{L \times M \times K \times P}$  since they will be exploited to formulate our second set of CE algorithms in the sequel. The remaining unfoldings can be deduced using a similar procedure by permuting the factor matrices in (14). This leads to the following factorizations to the other unfoldings

$$[\mathcal{Y}]_{(2)} = \mathbf{H} (\mathbf{E} \diamond \mathbf{S} \diamond \mathbf{G})^{\top} \in \mathbb{C}^{M \times LKP}, \quad (32)$$

$$[\mathcal{Y}]_{(3)} = \mathbf{S} (\mathbf{E} \diamond \mathbf{H} \diamond \mathbf{G})^{\top} \in \mathbb{C}^{K \times LMP}, \quad (33)$$

$$[\mathcal{Y}]_{(4)} = \mathbf{E} (\mathbf{S} \diamond \mathbf{H} \diamond \mathbf{G})^{\top} \in \mathbb{C}^{P \times LMK}. \quad (34)$$

In the following, we show that the channel matrices  $\mathbf{H}$  and  $\mathbf{G}$  can be also estimated when STI model is assumed. To this end, we propose to minimize the following quadrilinear LS fitting problem

$$\min_{\mathbf{G}, \mathbf{H}, \mathbf{E}} \left\| \tilde{\mathcal{Y}} - \mathcal{I}_{4,N} \times_1 \mathbf{G} \times_2 \mathbf{H} \times_3 \mathbf{S} \times_4 \mathbf{E} \right\|_{\text{F}}^2, \quad (35)$$

where  $\tilde{\mathcal{Y}} = \mathcal{Y} + \mathcal{V}$  as the noisy version of the received signal tensor  $\mathcal{Y}$ . Similar to the TALS-LTI algorithm, we also propose to solve this optimization problem by means of the ALS algorithm. Since the matrix  $\mathbf{S}$  is known at the receiver, the quadrilinear fitting problem in (35) is simplified to a trilinear fitting problem that reduces to iteratively minimize the following linear LS sub-problems formulated from (31), (32) and (34), respectively

$$\hat{\mathbf{G}} = \underset{\mathbf{G} | \mathbf{E}, \mathbf{H}}{\text{argmin}} \left\| [\tilde{\mathcal{Y}}]_{(1)} - \mathbf{G} (\mathbf{E} \diamond \mathbf{S} \diamond \mathbf{H})^{\top} \right\|_{\text{F}}^2, \quad (36)$$

$$\hat{\mathbf{H}} = \underset{\mathbf{H} | \mathbf{E}, \mathbf{G}}{\text{argmin}} \left\| [\tilde{\mathcal{Y}}]_{(2)} - \mathbf{H} (\mathbf{E} \diamond \mathbf{S} \diamond \mathbf{G})^{\top} \right\|_{\text{F}}^2, \quad (37)$$

$$\hat{\mathbf{E}} = \underset{\mathbf{E} | \mathbf{H}, \mathbf{G}}{\text{argmin}} \left\| [\tilde{\mathcal{Y}}]_{(4)} - \mathbf{E} (\mathbf{S} \diamond \mathbf{H} \diamond \mathbf{G})^{\top} \right\|_{\text{F}}^2. \quad (38)$$

---

**Algorithm 2: TALS-STI Algorithm**


---

1. Set  $i = 0$ ;  
Keep  $\mathbf{S}$  fixed;  
Initialize randomly the matrices  $\hat{\mathbf{H}}_{(i=0)}$  and  $\hat{\mathbf{E}}_{(i=0)}$ ;
  2.  $i \leftarrow i + 1$ ;
  3. Using (39), obtain an LS estimate of  $\hat{\mathbf{G}}_{(i)}$ :  

$$\hat{\mathbf{G}}_{(i)} = [\tilde{\mathcal{Y}}]_{(1)} \left[ \left( \hat{\mathbf{E}}_{(i-1)} \diamond \mathbf{S} \diamond \hat{\mathbf{H}}_{(i-1)} \right)^{\text{T}} \right]^{\dagger};$$
  4. Using (40), obtain an LS estimate of  $\hat{\mathbf{H}}_{(i)}$ :  

$$\hat{\mathbf{H}}_{(i)} = [\tilde{\mathcal{Y}}]_{(2)} \left[ \left( \hat{\mathbf{E}}_{(i-1)} \diamond \mathbf{S} \diamond \hat{\mathbf{G}}_{(i)} \right)^{\text{T}} \right]^{\dagger};$$
  5. Using (41), obtain an LS estimate of  $\hat{\mathbf{E}}_{(i)}$ :  

$$\hat{\mathbf{E}}_{(i)} = [\tilde{\mathcal{Y}}]_{(4)} \left[ \left( \mathbf{S} \diamond \hat{\mathbf{H}}_{(i)} \diamond \hat{\mathbf{G}}_{(i)} \right)^{\text{T}} \right]^{\dagger};$$
  6. Calculate the residual error  $\epsilon_{(i)} = \left\| [\tilde{\mathcal{Y}}]_{(1)} - [\hat{\mathcal{Y}}]_{(1)(i)} \right\|_{\text{F}}^2$   
where  $[\hat{\mathcal{Y}}]_{(1)(i)} = \hat{\mathbf{G}}_{(i)} \left( \hat{\mathbf{E}}_{(i)} \diamond \mathbf{S} \diamond \hat{\mathbf{H}}_{(i)} \right)^{\text{T}}$ ;
  7. Repeat Steps 2-6 until  $|\epsilon_{(i)} - \epsilon_{(i-1)}| \leq \delta$ .
- 

It follows from (36), (37), and (38) that the conditional LS updates of  $\hat{\mathbf{G}}$ ,  $\hat{\mathbf{H}}$ , and  $\hat{\mathbf{E}}$  are given by

$$\hat{\mathbf{G}} = [\tilde{\mathcal{Y}}]_{(1)} \left[ \left( \mathbf{E} \diamond \mathbf{S} \diamond \mathbf{H} \right)^{\text{T}} \right]^{\dagger}, \quad (39)$$

$$\hat{\mathbf{H}} = [\tilde{\mathcal{Y}}]_{(2)} \left[ \left( \mathbf{E} \diamond \mathbf{S} \diamond \mathbf{G} \right)^{\text{T}} \right]^{\dagger}, \quad (40)$$

$$\hat{\mathbf{E}} = [\tilde{\mathcal{Y}}]_{(4)} \left[ \left( \mathbf{S} \diamond \mathbf{H} \diamond \mathbf{G} \right)^{\text{T}} \right]^{\dagger}, \quad (41)$$

respectively. In the same way as in Algorithm 1, the updates of  $\hat{\mathbf{G}}$ ,  $\hat{\mathbf{H}}$ , and  $\hat{\mathbf{E}}$  are obtained by iteratively performing (39), (40) and (41) until the convergence. The proposed iterative TALS-STI algorithm is detailed in the pseudocode shown in Algorithm 2. For the complexity analysis of Algorithm 2, see Section IV.

*Remark 2:* In the application context of this work, the non-impaired RIS activation pattern matrix  $\mathbf{S}$  is assumed to be known at the receiver as indicated in the first step of Algorithms 1-2, respectively. This is a feasible assumption in accordance with the CE protocol shown in Fig. 2. Among different design possibilities, we set  $\mathbf{S}$  as a semi-unitary matrix satisfying  $\mathbf{S}^{\text{H}}\mathbf{S} = K\mathbf{I}_N$ . According to [33], a good choice is to consider  $\mathbf{S}$  as a deterministic truncated discrete Fourier transform (DFT) matrix. This choice guarantees a good performance of the proposed algorithms since the correlation properties of the additive noise are not affected during the estimation processing. More details on the optimal design of  $\mathbf{S}$  are found in [46]. Moreover, despite the iterative nature of the proposed TALS-LTI and TALS-STI algorithms, the convergence to the global minimum is always achieved within a few iterations (usually less than 80 iterations as verified in our simulation results) due to the knowledge of  $\mathbf{S}$  that remains fixed during the iterations.

### C. HOSVD Algorithm for RIS under STI (HOSVD-STI)

We now derive a closed-form solution based on higher order singular value decomposition (HOSVD) for CE under

the STI model. According to (33), the transpose of the 3-mode unfolding of  $\mathcal{Y}$  is denoted by

$$[\tilde{\mathcal{Y}}]_{(3)}^{\text{T}} = (\mathbf{E} \diamond \mathbf{H} \diamond \mathbf{G}) \mathbf{S}^{\text{T}}. \quad (42)$$

The first processing step at the receiver is to apply a bilinear time-domain matched-filtering by multiplying both sides in (42) by the pseudo-inverse of  $\mathbf{S}^{\text{T}}$ , resulting in

$$\tilde{\mathbf{Y}} \approx \mathbf{E} \diamond \mathbf{H} \diamond \mathbf{G} \in \mathbb{C}^{LMP \times N}, \quad (43)$$

where  $\tilde{\mathbf{Y}} = [\tilde{\mathcal{Y}}]_{(3)}^{\text{T}} (\mathbf{S}^{\text{T}})^{\dagger}$ . From (43), decoupled estimates of the channel matrices and RIS imperfections can be obtained by separating each factor matrix in the Khatri-Rao product. In this sense, the estimates can be obtained by minimizing the following cost function

$$\min_{\mathbf{G}, \mathbf{H}, \mathbf{E}} \left\| \tilde{\mathbf{Y}} - \mathbf{E} \diamond \mathbf{H} \diamond \mathbf{G} \right\|_{\text{F}}^2. \quad (44)$$

Here, we propose to solve this problem by means of multiple rank-one tensor approximations via the HOSVD [36]. To this end, let us define  $\tilde{\mathbf{Y}} = [\tilde{\mathbf{y}}_1, \dots, \tilde{\mathbf{y}}_N] \in \mathbb{C}^{LMP \times N}$  where the  $n$ -th column of  $\tilde{\mathbf{Y}}$  can be written as  $\tilde{\mathbf{y}}_n = \mathbf{e}_n \otimes \mathbf{h}_n \otimes \mathbf{g}_n \in \mathbb{C}^{LMP \times 1}$ , where  $\mathbf{e}_n \in \mathbb{C}^{P \times 1}$ ,  $\mathbf{h}_n \in \mathbb{C}^{M \times 1}$ , and  $\mathbf{g}_n \in \mathbb{C}^{L \times 1}$  are the  $n$ -th column of  $\mathbf{E}$ ,  $\mathbf{H}$ , and  $\mathbf{G}$ , respectively. Using the equivalence property in (3) that relates the Kronecker product to the outer product, we can rewrite  $\tilde{\mathbf{y}}_n$  as

$$\tilde{\mathbf{y}}_n = \text{vec}(\mathbf{g}_n \circ \mathbf{h}_n \circ \mathbf{e}_n) \in \mathbb{C}^{LMP \times 1}. \quad (45)$$

that represents the vectorized form of the following third-order rank-one tensor

$$\tilde{\mathcal{Y}}_n = \mathbf{g}_n \circ \mathbf{h}_n \circ \mathbf{e}_n \in \mathbb{C}^{L \times M \times P}. \quad (46)$$

Thus, the optimization problem in (44) is equivalent to finding the estimates of  $\mathbf{H}$ ,  $\mathbf{G}$  and  $\mathbf{E}$  that minimize a set of  $N$  rank-one tensor approximations, i.e.,

$$\left( \hat{\mathbf{G}}, \hat{\mathbf{H}}, \hat{\mathbf{E}} \right) = \underset{\mathbf{G}, \mathbf{H}, \mathbf{E}}{\text{argmin}} \sum_{n=1}^N \left\| \tilde{\mathcal{Y}}_n - \mathbf{g}_n \circ \mathbf{h}_n \circ \mathbf{e}_n \right\|_{\text{F}}^2. \quad (47)$$

Let us introduce the HOSVD of  $\tilde{\mathcal{Y}}_n$  as

$$\tilde{\mathcal{Y}}_n = \mathcal{G}_n \times_1 \mathbf{U}_n^{(1)} \times_2 \mathbf{U}_n^{(2)} \times_3 \mathbf{U}_n^{(3)} \in \mathbb{C}^{L \times M \times P}, \quad (48)$$

where  $\mathbf{U}_n^{(1)} \in \mathbb{C}^{L \times L}$ ,  $\mathbf{U}_n^{(2)} \in \mathbb{C}^{M \times M}$ , and  $\mathbf{U}_n^{(3)} \in \mathbb{C}^{P \times P}$  are unitary matrices, while  $\mathcal{G}_n \in \mathbb{C}^{L \times M \times P}$  denotes the HOSVD core tensor. The estimates of the vectors  $\mathbf{g}_n$ ,  $\mathbf{h}_n$  and  $\mathbf{e}_n$  that solve the LS problem in (47) can be obtained by truncating the HOSVD of  $\tilde{\mathcal{Y}}_n$  to its dominant rank-one component, yielding

$$\begin{aligned} \hat{\mathbf{g}}_n &= \sqrt[3]{(\mathcal{G}_n)_{1,1,1}} \cdot \mathbf{u}_{1,n}^{(1)}, \\ \hat{\mathbf{h}}_n &= \sqrt[3]{(\mathcal{G}_n)_{1,1,1}} \cdot \mathbf{u}_{1,n}^{(2)}, \\ \hat{\mathbf{e}}_n &= \sqrt[3]{(\mathcal{G}_n)_{1,1,1}} \cdot \mathbf{u}_{1,n}^{(3)}, \end{aligned} \quad (49)$$

where  $\mathbf{u}_{1,n}^{(1)} \in \mathbb{C}^{L \times 1}$ ,  $\mathbf{u}_{1,n}^{(2)} \in \mathbb{C}^{M \times 1}$ , and  $\mathbf{u}_{1,n}^{(3)} \in \mathbb{C}^{P \times 1}$  are the first higher-order singular vectors, i.e., the first column of  $\mathbf{U}_n^{(1)}$ ,  $\mathbf{U}_n^{(2)}$ , and  $\mathbf{U}_n^{(3)}$ , respectively. Here,  $(\mathcal{G}_n)_{1,1,1}$  is the first element of the core tensor  $\mathcal{G}_n$ . The estimates of  $\hat{\mathbf{G}}$ ,  $\hat{\mathbf{H}}$ , and  $\hat{\mathbf{E}}$  are obtained column by column from (49) for

---

**Algorithm 3: HOSVD-STI Algorithm**


---

for  $n = 1, \dots, N$

1. Rearrange the  $n$ -th column of  $\tilde{\mathbf{Y}}$  in Equation (43) as the rank-one tensor  $\tilde{\mathcal{Y}}_n$  in Equation (46);

2. HOSVD procedure

2.1 Compute  $\mathbf{U}_n^{(1)}$  as the  $L$  left singular vectors of  $[\tilde{\mathcal{Y}}_n]_{(1)}$ :  
 $[\tilde{\mathcal{Y}}_n]_{(1)} = \mathbf{U}_n^{(1)} \cdot \Sigma_n^{(1)} \cdot \mathbf{V}_n^{(1)\text{H}}$ ;

2.2 Compute  $\mathbf{U}_n^{(2)}$  as the  $M$  left singular vectors of  $[\tilde{\mathcal{Y}}_n]_{(2)}$ :  
 $[\tilde{\mathcal{Y}}_n]_{(2)} = \mathbf{U}_n^{(2)} \cdot \Sigma_n^{(2)} \cdot \mathbf{V}_n^{(2)\text{H}}$ ;

2.3 Compute  $\mathbf{U}_n^{(3)}$  as the  $P$  left singular vectors of  $[\tilde{\mathcal{Y}}_n]_{(3)}$ :  
 $[\tilde{\mathcal{Y}}_n]_{(3)} = \mathbf{U}_n^{(3)} \cdot \Sigma_n^{(3)} \cdot \mathbf{V}_n^{(3)\text{H}}$ ;

2.4 Compute the HOSVD core tensor  $\mathcal{G}_n$  as:

$$\mathcal{G}_n = \tilde{\mathcal{Y}}_n \times_1 \mathbf{U}_n^{(1)\text{H}} \times_2 \mathbf{U}_n^{(2)\text{H}} \times_3 \mathbf{U}_n^{(3)\text{H}};$$

end procedure

3. Obtain the estimates for  $\hat{\mathbf{g}}_n$ ,  $\hat{\mathbf{h}}_n$  and  $\hat{\mathbf{e}}_n$  from Equations (49);  
 end

4. Return the matrices  $\hat{\mathbf{G}} = [\hat{\mathbf{g}}_1, \dots, \hat{\mathbf{g}}_N]$ ,  $\hat{\mathbf{H}} = [\hat{\mathbf{h}}_1, \dots, \hat{\mathbf{h}}_N]$   
 and  $\hat{\mathbf{E}} = [\hat{\mathbf{e}}_1, \dots, \hat{\mathbf{e}}_N]$ .

---

the  $N$  columns of  $\tilde{\mathbf{Y}}$  in (43). In other words, a total of  $N$  rank-one tensor approximations via HOSVD are necessary to obtain the full estimates of the matrices  $\hat{\mathbf{G}} = [\hat{\mathbf{g}}_1, \dots, \hat{\mathbf{g}}_N]$ ,  $\hat{\mathbf{H}} = [\hat{\mathbf{h}}_1, \dots, \hat{\mathbf{h}}_N]$  and  $\hat{\mathbf{E}} = [\hat{\mathbf{e}}_1, \dots, \hat{\mathbf{e}}_N]$  in a closed-form manner. The implementation steps of the proposed closed-form HOSVD-STI algorithm are summarized in Algorithm 3. For the complexity analysis of Algorithm 3, see Section IV.

#### D. Handling frames with different sizes

For notation convenience and simplicity, we have considered frames with equal size, i.e., with the same number  $K$  of blocks. However, the proposed method can be easily adapted to processing frames with different sizes. Considering the STI model, let us assume that the  $p$ -th frame is composed of  $K_p$  blocks and denote  $\mathbf{S}_p = [\mathbf{s}[1], \dots, \mathbf{s}[K_p]]^T \in \mathbb{C}^{K_p \times N}$  as the RIS phase shift matrix associated with the  $p$ -th frame,  $p = 1, \dots, P$ . We can rewrite (14) as

$$\mathbf{Y}[p, k_p] = \mathbf{G}\mathbf{D}_p(\mathbf{E})\mathbf{D}_{k_p}(\mathbf{S}_p)\mathbf{H}^T + \mathbf{V}[p, k_p]. \quad (50)$$

Applying the  $\text{vec}(\cdot)$  operator on  $\mathbf{Y}[p, k_p]$  yields

$$\mathbf{y}[p, k_p] = (\mathbf{H} \diamond \mathbf{G})(\mathbf{e}[p] \odot \mathbf{s}[k_p]) + \bar{\mathbf{v}}[p, k_p] \in \mathbb{C}^{LM \times 1},$$

where  $\bar{\mathbf{v}}[p, k_p] = \text{vec}(\mathbf{V}[p, k_p])$ . Concatenating the  $K_p$  blocks of the  $p$ -frame leads to

$$\begin{aligned} \mathbf{Y}_p &= [\mathbf{y}[p, 1], \dots, \mathbf{y}[p, K_p]] \in \mathbb{C}^{LM \times K_p} \\ &= (\mathbf{H} \diamond \mathbf{G})[(\mathbf{e}[p] \odot \mathbf{s}[1]), \dots, (\mathbf{e}[p] \odot \mathbf{s}[K_p])] + \bar{\mathbf{V}}[p] \\ &= (\mathbf{H} \diamond \mathbf{G})\mathbf{D}_p(\mathbf{E})\mathbf{S}_p^T + \bar{\mathbf{V}}[p], \end{aligned} \quad (51)$$

where  $\bar{\mathbf{V}}[p] = [\bar{\mathbf{v}}[p, 1], \dots, \bar{\mathbf{v}}[p, K_p]]$ . Since the nominal RIS phase shift matrix is known at the receiver, right-filtering the received signal at the  $p$ -th frame yields

$$\bar{\mathbf{Y}}_p = \mathbf{Y}_p(\mathbf{S}_p^T)^\dagger \in \mathbb{C}^{LM \times N} \quad (52)$$

$$\approx (\mathbf{H} \diamond \mathbf{G})\mathbf{D}_p(\mathbf{E}), \quad p = 1, \dots, P. \quad (53)$$

Stacking the filtered signals for all  $P$  frames and using property (1), we obtain

$$\bar{\mathbf{Y}} = \begin{bmatrix} \bar{\mathbf{Y}}_1 \\ \vdots \\ \bar{\mathbf{Y}}_P \end{bmatrix} \approx \mathbf{E} \diamond \mathbf{H} \diamond \mathbf{G} \in \mathbb{C}^{LMP \times N}. \quad (54)$$

Note that (54) has the same structure as (43). Hence, the factor matrices  $\mathbf{E}$ ,  $\mathbf{H}$  and  $\mathbf{G}$  can be estimated by following exactly the same steps given in (44)-(49) by means of the HOSVD algorithm (Algorithm 3).

#### IV. IDENTIFIABILITY AND COMPUTATIONAL COMPLEXITY

In this section, we examine the identifiability aspects and the computational complexity associated with the proposed tensor-based TALS-LTI, TALS-STI, and HOSVD-STI algorithms<sup>3</sup>.

1) *TALS-LTI algorithm*: The uniqueness of the LS estimates of  $\hat{\mathbf{G}}$ ,  $\hat{\mathbf{H}}$ , and  $\hat{\mathbf{e}}$  requires that  $\text{diag}(\mathbf{e})(\mathbf{S} \diamond \mathbf{H})^T \in \mathbb{C}^{N \times KM}$ ,  $\text{diag}(\mathbf{e})(\mathbf{S} \diamond \mathbf{G})^T \in \mathbb{C}^{N \times KL}$  and  $(\mathbf{S} \diamond \mathbf{H} \diamond \mathbf{G}) \in \mathbb{C}^{KLM \times N}$  are full row-rank. This means that the conditions  $N \leq KM$ ,  $N \leq KL$ , and  $N \leq KLM$  should be jointly satisfied. By combining these necessary and sufficient conditions, we obtain the lower bound on the number  $K$  of time blocks necessary for CE such that Steps 3, 4, and 5 in Algorithm 1 yield a unique solution:  $K \geq \lceil N / \min(L, M) \rceil$ .

2) *TALS-STI algorithm*: We can note from (39), (40), and (41) that unique estimates of  $\hat{\mathbf{G}}$ ,  $\hat{\mathbf{H}}$ , and  $\hat{\mathbf{E}}$  in the LS sense requires that  $(\mathbf{E} \diamond \mathbf{S} \diamond \mathbf{H})^T \in \mathbb{C}^{N \times KMP}$ ,  $(\mathbf{E} \diamond \mathbf{S} \diamond \mathbf{G})^T \in \mathbb{C}^{N \times KLP}$ , and  $(\mathbf{S} \diamond \mathbf{H} \diamond \mathbf{G})^T \in \mathbb{C}^{N \times KLM}$  are full row-rank to be right-invertible. This means the conditions  $N \leq KMP$ ,  $N \leq KLP$ , and  $N \leq KLM$  should be satisfied. The combination of these inequalities leads to the following necessary and sufficient condition to be satisfied:  $K \geq \lceil N / \min(MP, LP, LM) \rceil$ .

This condition establishes the lower-bound on the required number of time-blocks  $K$  such that Steps 3, 4, and 5 in Algorithm 2 provide unique solutions when STI are assumed.

3) *HOSVD-STI algorithm*: In contrast to the iterative TALS-LTI and TALS-STI algorithms in which three LS conditions must be jointly satisfied, the proposed HOSVD-STI algorithm is a closed-form solution requiring only that the RIS activation pattern matrix  $\mathbf{S} \in \mathbb{C}^{K \times N}$  has full column-rank in order to guarantee the uniqueness in the LS sense when the bilinear time-domain matched-filtering preprocessing is performed at the receiver side, as indicated in (43). This means that  $K \geq N$  should be satisfied.

4) *Computational complexity*: As can be observed in Algorithms 1-2, the computational complexity of the proposed TALS-LTI and TALS-STI algorithms are dominated by the cost associated with the computation of the matrix pseudo-inverses in three LS update steps that calculate the estimates of the channels and imperfection matrices in an iterative and alternating way. Therefore, the computational complexity of the TALS-LTI and TALS-STI algorithms are  $\mathcal{O}(N^2K[M + L + ML])$  and  $\mathcal{O}(N^2K[PM + PL + ML])$

<sup>3</sup>Since  $\mathbf{S}$  is known at the receiver, the estimated factor matrices  $\hat{\mathbf{G}}$ ,  $\hat{\mathbf{H}}$  and  $\hat{\mathbf{E}}$  do not suffer from column permutation ambiguity. The scaling ambiguity affecting the columns of the estimated matrices can be eliminated with a simple normalization procedure, as performed in [47] and [33].

per iteration, respectively. Regarding the proposed HOSVD-STI in Algorithm 3, its computational complexity is dominated by the HOSVD of the third-order rank-one tensor in (46), which is equivalent to computing the truncated SVDs of its 1-mode, 2-mode, and 3-mode unfolding matrices to rank-one. These truncated SVDs are repeated  $N$  times. Therefore, the HOSVD-STI algorithm has a complexity  $\mathcal{O}(NMLP)$ , which is clearly less than that of the TALS-LTI and TALS-STI algorithms. In particular, as opposed to Algorithms 1-2, where the computational complexity is proportional to  $N^2$ , in Algorithm 3 the complexity scales with the RIS size  $N$  linearly. As a result, compared to Algorithms 1-2, the relative gain of Algorithm 3, in terms of complexity, increases rapidly as the number of RIS elements increases.

To summarize, we can note that the TALS-STI algorithm has less restrictive requirements on the minimum number  $K$  of time blocks necessary for the CE. On the other hand, the HOSVD-STI algorithm involves computing  $N$  rank-one tensor approximation steps via the HOSVD on the post-filtered signal according to (47). These steps can be parallelized if more than one processor is available, leading to a considerable reduction in the processing delay associated with CE, in comparison to the TALS-STI algorithm, while being a less complex solution. Hence, we can conclude that the TALS-STI algorithm offers more flexibility on the choices of  $K$ , being able to operate with a smaller number of blocks compared to the HOSVD-STI, while the latter is more attractive in scenarios with low latency requirements. Moreover, the computational complexity of the HOSVD-STI scales linearly with the RIS size  $N$  while that of TALS increases proportionally to  $N^2$ . Hence, there is a tradeoff between computational complexity and operation conditions offered by the proposed tensor-based algorithms.

## V. SIMULATION RESULTS

In this section, we present the results for different parameters to study the proposed schemes from different perspectives. Specifically, we present the simulation results for performance evaluation of our proposed tensor-based algorithms in terms of computational complexity and estimation accuracy of the involved channels and imperfections while comparing with benchmark approaches. The results presented here are averaged over  $R=3000$  independent Monte Carlo runs. Each run corresponds to a different realization of the involved communication channels, RIS patterns, impairment parameters, and noise. We have designed the RIS pattern matrix  $\mathbf{S}$  as a DFT matrix. The amplitude and phase impairments parameters embedded in the vector  $\mathbf{e}$  and in the matrix  $\mathbf{E}$  follow a uniform distribution between  $[0, 1]$  and between  $[0, 2\pi]$ , respectively. The location of the unknown  $N_B$  impaired elements are assumed to be random with occurrence probability  $R_B$ , yielding  $N_B = NR_B$  impaired elements at the RIS in each simulated setup. The metric used to evaluate the estimation accuracy is the normalized mean square error (NMSE) between the true and estimated matrices that provides a relative measure for the estimation error of the proposed algorithms. For the estimated

channel  $\hat{\mathbf{H}}$ , we define

$$\text{NMSE}(\hat{\mathbf{H}}) = \frac{1}{R} \sum_{r=1}^R \frac{\|\mathbf{H}^{(r)} - \hat{\mathbf{H}}^{(r)}\|_{\text{F}}^2}{\|\mathbf{H}^{(r)}\|_{\text{F}}^2}, \quad (55)$$

where  $\mathbf{H}^{(r)}$  and  $\hat{\mathbf{H}}^{(r)}$  denote the true channel and its estimate both related to the  $r$ -th run, respectively. Similar definitions as in (55) apply to the estimates of  $\hat{\mathbf{G}}$ ,  $\hat{\mathbf{E}}$  and  $\hat{\mathbf{e}}$ . Finally, note that while we present the simulation results for a set of parameter settings, we have tested the results for a broad range of parameter settings and observed the same qualitative conclusions as those presented.

For simulation purposes, we assume that one row of each factor matrix, i.e.,  $\mathbf{G}$ ,  $\mathbf{H}$ ,  $\mathbf{E}$  is known at the receiver in order to remove the scaling ambiguity present on the proposed methods. However, note that in the practical use of the estimated matrices, the scaling ambiguities of  $\hat{\mathbf{G}}$ ,  $\hat{\mathbf{H}}$ , and  $\hat{\mathbf{E}}$ , cancel each other, not affecting, for example, a data detection procedure [24], [48]. More specifically, after the TALS and HOSVD algorithms, the estimated factors are related to the true ones with the following relationships:

$$\hat{\mathbf{G}} = \mathbf{G} \text{diag}(\lambda^{(\mathbf{G})}), \quad \hat{\mathbf{H}} = \mathbf{H} \text{diag}(\lambda^{(\mathbf{H})}), \quad \hat{\mathbf{E}} = \mathbf{E} \text{diag}(\lambda^{(\mathbf{E})}),$$

where  $\lambda^{(\mathbf{X})} = [\lambda_1^{(\mathbf{X})}, \dots, \lambda_1^{(\mathbf{X})}]^T \in \mathbb{C}^{N \times 1}$ , for  $\mathbf{X} = \{\mathbf{G}, \mathbf{H}, \mathbf{E}\}$ , is the vector containing the scaling factors of the estimated matrices, with  $\text{diag}(\lambda^{(\mathbf{G})}) \text{diag}(\lambda^{(\mathbf{H})}) \text{diag}(\lambda^{(\mathbf{E})}) \approx \mathbf{I}_N$  (is equal on the ideal noiseless case). Consequently, in order to remove the effect of  $\lambda^{(\mathbf{X})}$ , the receiver should have the *a priori* knowledge of one row of each factor matrix. Assuming as known the first row of  $\mathbf{G}$ ,  $\mathbf{H}$ ,  $\mathbf{E}$ , the scaling factor can be estimated as

$$\begin{aligned} \lambda^{(\mathbf{G})} &= \hat{\mathbf{G}}_{(1,:)} \oslash \mathbf{G}_{(1,:)}, & \lambda^{(\mathbf{H})} &= \hat{\mathbf{H}}_{(1,:)} \oslash \mathbf{H}_{(1,:)}, \\ \lambda^{(\mathbf{E})} &= \hat{\mathbf{E}}_{(1,:)} \oslash \mathbf{E}_{(1,:)}, \end{aligned}$$

where " $\oslash$ " stands for element-wise division.

### A. TALS-LTI Performance

We first examine, in Figs. 4 and 5, the performance of the proposed TALS-LTI algorithm. These plots show the NMSE and computational complexity in terms of floating-point operations (FLOPS) assuming i.i.d. Rayleigh fading channels. As a benchmark, we compare our TALS-LTI algorithm with the method proposed in [24], which is also a PARAFAC-based algorithm but formulated to the ideal case in which no impairments affect the RIS elements. Additionally, as a lower-bound for comparison, we also plot the performance of the *clairvoyant* LS estimators of  $\hat{\mathbf{H}}$ ,  $\hat{\mathbf{G}}$  and  $\hat{\mathbf{e}}$  in (23), (24) and (25) obtained when the true factor matrices in the right-hand side of these equations are perfectly known.

From Figs. 4a and 4b, we can observe that the method in [24] is not suitable to tackle the CE problem when RIS impairments are present. In contrast, our proposed TALS-LTI algorithm provides accurate estimates in which the NMSE of the estimated channels decreases linearly when the SNR increases, and is not sensitive to the number of impaired elements at the RIS. For instance, the TALS-LTI presents constant gaps when compared to the lower-bound LS estimator

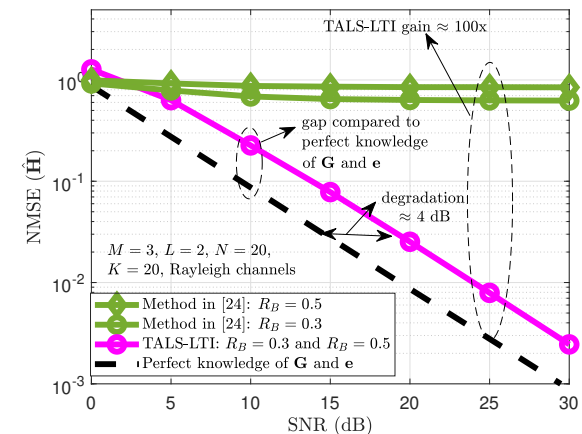
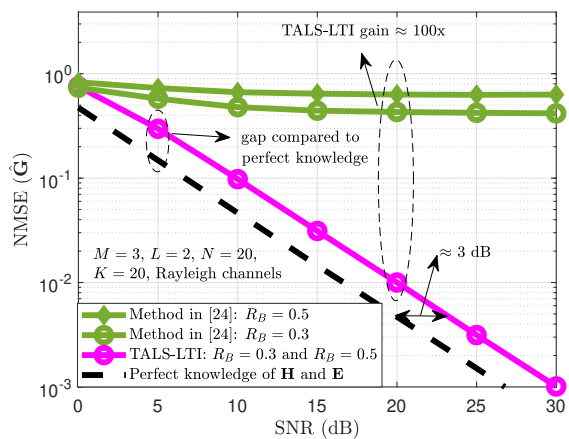
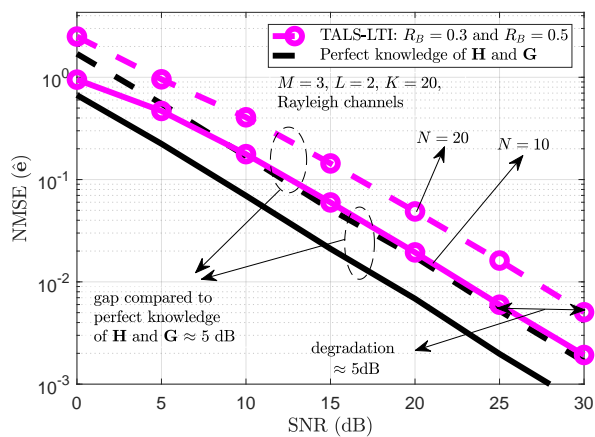
(a) NMSE of  $\hat{\mathbf{H}}$  versus SNR (dB).(b) NMSE of  $\hat{\mathbf{G}}$  versus SNR (dB).(c) NMSE of  $\hat{\mathbf{e}}$  versus SNR (dB).

Fig. 4: NMSE performance of TALS-LTI versus SNR (dB).

equal to 4 dB and 3 dB, providing satisfactory performance in terms of the CE for all simulated SNR range. Also, in contrast to the method in [24], the TALS-LTI accurately estimates the RIS impairments that are treated as independent variables estimated beyond the involved channels, as illustrated in Fig. 4c.

In terms of computational complexity, we can see from

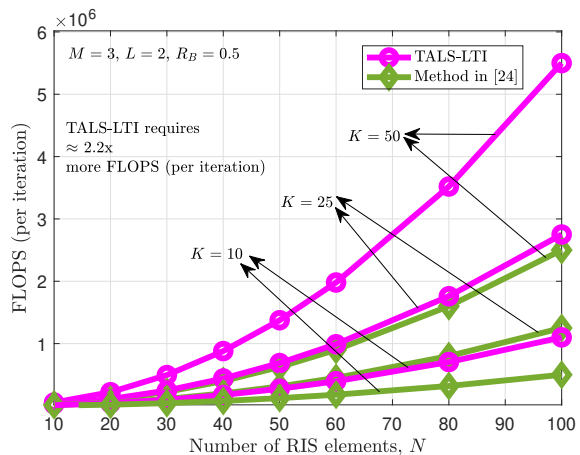


Fig. 5: Number of FLOPS required by the TALS-LTI algorithm versus the number of the RIS elements.

Fig. 5 that the TALS-LTI has a higher complexity than the competitor method requiring approximately 2.2x more FLOPS per iteration. This happens because the TALS-LTI has one more updating step (per iteration) to estimate the RIS imperfections compared to the method in [24] that does not perform the estimation of imperfections. Also, the complexity of both approaches increases with the number  $N$  of RIS elements and the number  $K$  of time blocks.

### B. TALS-STI and HOSVD-STI Performance

Here, we evaluate the performance of the proposed TALS-STI and HOSVD-STI algorithms assuming i.i.d. Rayleigh fading channels and a typical mmWave propagation environment. For the mmWave setup, we assume that the transmitter and the receiver are equipped with half-wavelength spaced uniform linear arrays while the RIS has half-wavelength spaced reflecting elements in a uniform rectangular grid. In this case, the channel matrices are generated according to the widely used geometric channel model [49]. The number of propagation paths is set to 1 in the Tx-RIS link and to 2 in the RIS-Rx link, respectively. The complex channel gains follow uniform distributions. The lower-bound LS estimators of  $\hat{\mathbf{H}}$ ,  $\hat{\mathbf{G}}$  and  $\hat{\mathbf{E}}$  are obtained similarly to Section V-A, but now from (39), (40) and (41), respectively.

From Fig. 6, similar conclusions to the results in Fig. 4, in terms of CE performance, can be made by comparing the proposed TALS-STI and HOSVD-STI algorithms with the method in [24]. However, more accurate estimates for the channels and impairments are obtained when the mmWave propagation scenario is considered. In this experiment, the TALS-STI and HOSVD-STI present, respectively, constant gaps of approximately 1 dB and 2 dB, compared to the lower-bound LS estimator for the considered range of SNR, confirming the effectiveness of the proposed tensor-based algorithms in terms of estimation accuracy. Similar results are obtained for the proposed TALS-LTI algorithm but omitted here due to space limitation. Also, we see from Fig. 6c that in the low/medium SNR regime, the TALS-STI algorithm outperforms the HOSVD-STI one in terms of imperfections

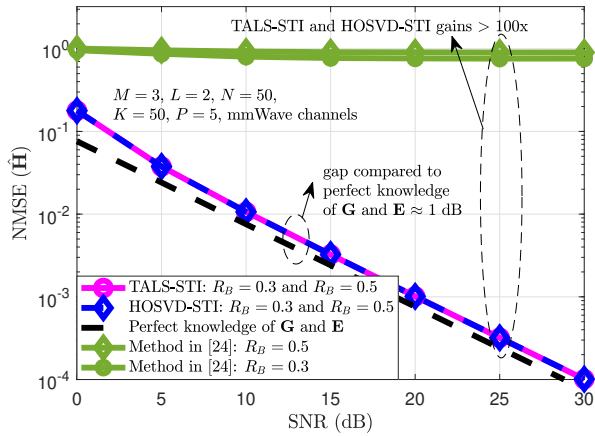
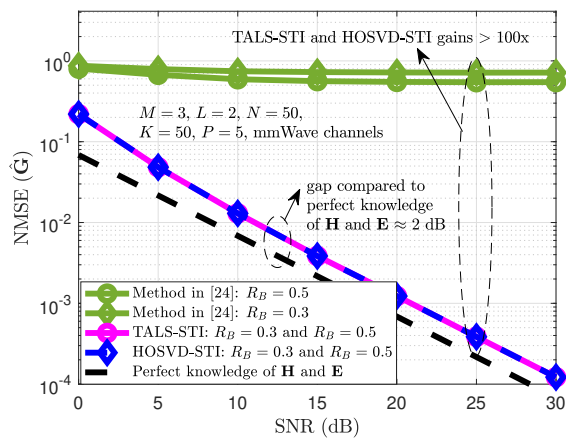
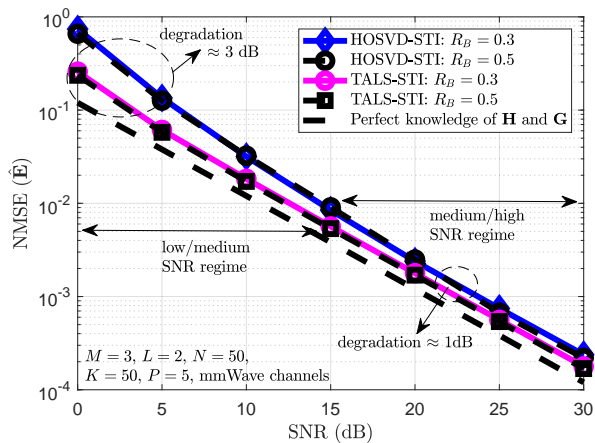
(a) NMSE of  $\hat{\mathbf{H}}$  versus SNR (dB).(b) NMSE of  $\hat{\mathbf{G}}$  versus SNR (dB).(c) NMSE of  $\hat{\mathbf{E}}$  versus SNR (dB).

Fig. 6: NMSE performance of the TALS-STI and HOSVD-STI algorithms versus the SNR (dB) for  $M = 3$  transmit antennas,  $L = 2$  receive antennas,  $N = 50$  elements with  $\{10, 5\}$  elements placed on the  $\{x, y\}$ -axes RIS elements.

estimation, indicating that the TALS-STI algorithm becomes preferable with a considerable gain in the low SNR regime when complexity issues are not taken into account. The tradeoff between computational complexity and estimation

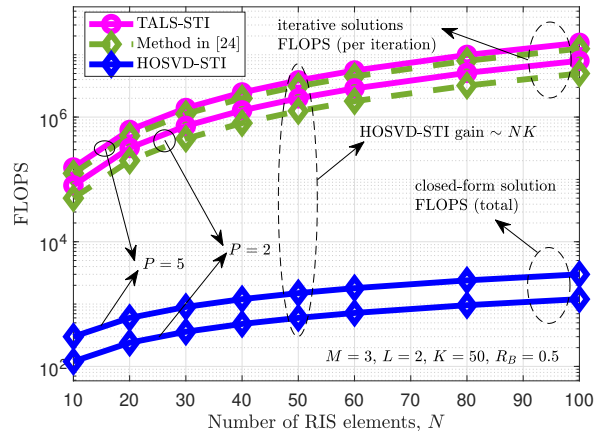


Fig. 7: Number of FLOPS required by the TALS-STI and HOSVD-STI algorithms versus the number of RIS elements.

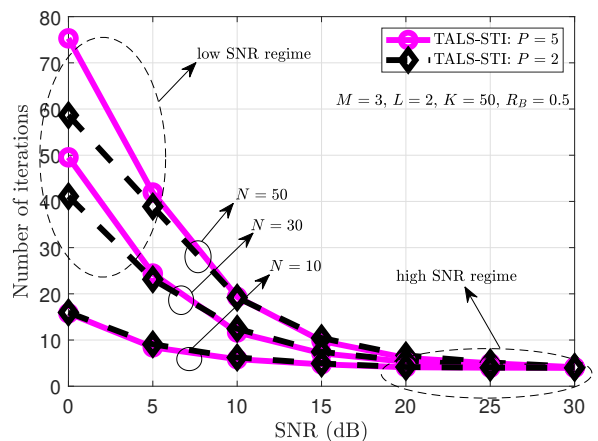


Fig. 8: Number of iterations required by the TALS-STI algorithm versus SNR (dB).

performance is analyzed in the sequel. The presented result indicates that the proposed algorithms are able to work with high accuracy under different propagation environments and kinds of imperfections, i.e., our approaches are general techniques that provide accurate estimates for different channel models.

In Fig. 7, we evaluate the computational complexity (in terms of FLOPS) of the TALS-STI and HOSVD-STI algorithms. We can see that the HOSVD-STI is less complex than TALS-STI for different values of RIS elements  $N$  and frames  $P$  since it is a closed-form solution for joint channel and imperfections estimation. The HOSVD-STI algorithm provides a remarkable gain of the order of  $NK$  FLOPS compared to the TALS-STI one. It can be seen that the complexity of both methods grows when the number of RIS elements  $N$  and frames  $P$  increases, which is an expected result since the number of entries in  $\mathbf{H}$ ,  $\mathbf{G}$ , and  $\mathbf{E}$  also increases with  $N$  and  $P$ . However, in contrast to the HOSVD-STI, which is a closed-form solution, for a complete analysis of the overall complexity of the proposed techniques, Fig. 8 shows the number of iterations necessary for the convergence of the TALS-STI algorithm considering different values of  $N$  and  $P$ . It can be seen that the TALS-STI algorithm rapidly converges

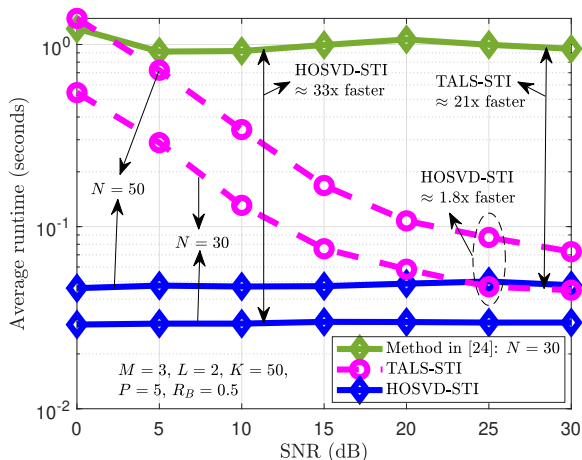
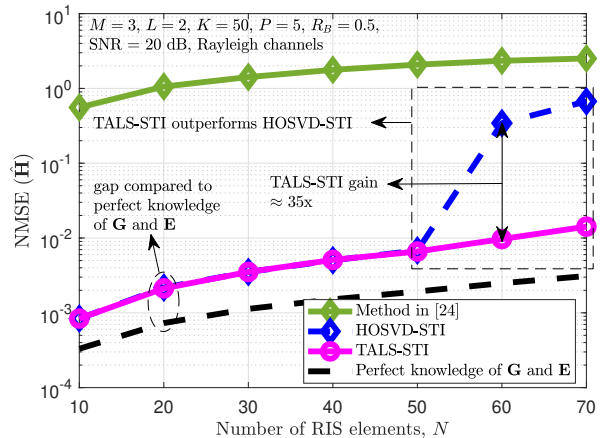


Fig. 9: Average runtime (in seconds) for the TALS-STI and HOSVD-STI algorithms versus the SNR (dB).

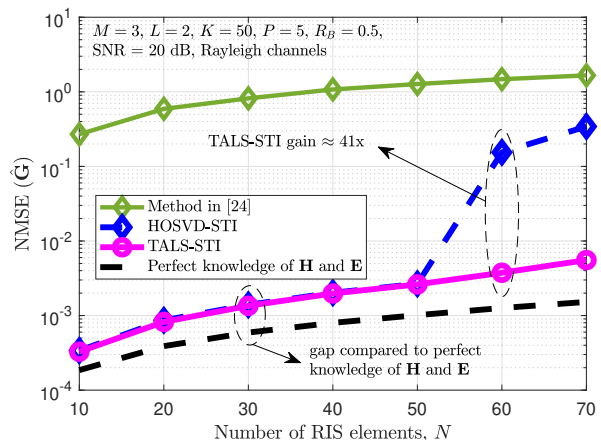
due the knowledge of the matrix  $\mathbf{S}$ . Also, the number of iterations required for the convergence decreases as a function of the SNR. In the high SNR regime, the convergence of the proposed TALS-STI algorithm is no more sensitive to  $N$ ,  $P$ , and SNR values. When the SNR is higher than 20 dB, its convergence is quickly achieved within approximately 5 iterations.

In Fig. 9, we evaluate the overall computational complexity of the TALS-STI and HOSVD-STI algorithms using as a metric the average runtime (in seconds). This metric considers the number of iterations for convergence, making it possible to compare the complexity between iterative and closed-form solutions. It can be seen that the runtime grows when the number  $N$  of RIS elements increases, confirming the results shown in Fig. 7. The runtime required by HOSVD-STI is not sensitive to the SNR since it is a closed-form algorithm. On the other hand, the runtime of the TALS-STI algorithm decreases with the SNR as it is an iterative algorithm, achieving performance close to HOSVD-STI algorithm in the high SNR regime thanks to its rapid convergence (Fig. 8).

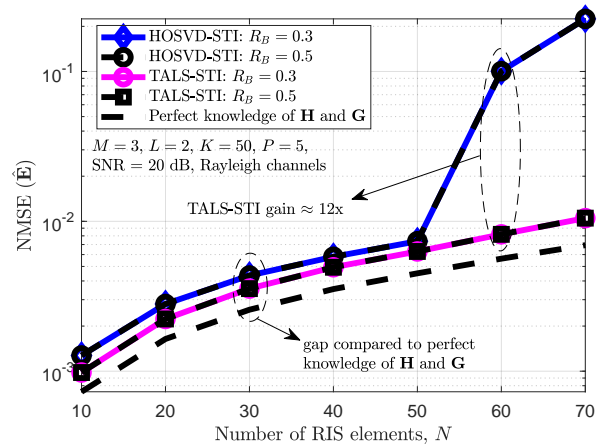
We can conclude that TALS-STI and HOSVD-STI algorithms outperform the method in [24] in terms of both CE accuracy and overall computational complexity. Due to the RIS imperfections, the method in [24] does not estimate channels properly and has very slow convergence which directly increases its runtime. However, the TALS-STI can operate under more flexible choices for the number  $K$  of time-blocks for CE compared to HOSVD-STI (see Fig. 10). In Fig. 10, we compare the NMSE by varying the number  $N$  of RIS elements and observe that for  $K = 50$  blocks and  $N > 50$  elements, the condition  $K \geq N$  required by the HOSVD-STI is not satisfied (please see Section IV), which leads to significant performance degradation. In this case, the TALS-STI algorithm is the preferred solution in terms of estimation accuracy. Therefore, a tradeoff between overall computational complexity, estimation performance, and operation conditions for the proposed solutions can be observed. Thus, the TALS-STI may be attractive when more flexible choices for the



(a) NMSE of  $\hat{\mathbf{H}}$  versus  $N$ .



(b) NMSE of  $\hat{\mathbf{G}}$  versus  $N$ .



(c) NMSE of  $\hat{\mathbf{E}}$  versus  $N$ .

Fig. 10: NMSE performance of the TALS-STI and HOSVD-STI algorithms versus the number of RIS elements.

number  $K$  of time-blocks for CE are required, while the HOSVD-STI is preferred, especially when low processing delay is desired. We can also observe that when  $N$  increases, the CE performance degrades. This is a coherent result since the channel components and imperfections coefficients to be estimated also grow.

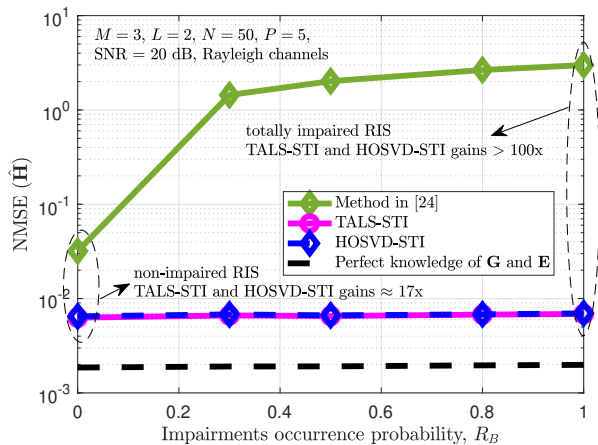
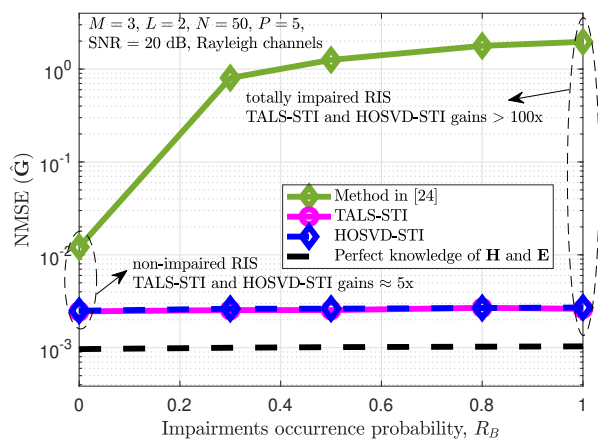
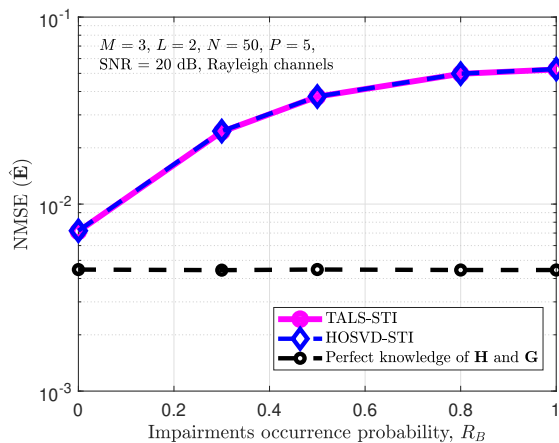
(a) NMSE of  $\hat{\mathbf{H}}$  versus  $R_B$ .(b) NMSE of  $\hat{\mathbf{G}}$  versus  $R_B$ .(c) NMSE of  $\hat{\mathbf{E}}$  versus  $R_B$ .

Fig. 11: NMSE performance of the TALS-STI and HOSVD-STI algorithms versus the impairments occurrence probability  $R_B$ .

In Fig. 11, we evaluate the NMSE as a function of the impairments occurrence probability  $R_B$ . It can be seen that, in terms of CE accuracy, for a broad range of parameter settings, our proposed methods are not sensitive to the number of impaired elements at the RIS. This is because the imperfections matrix is estimated as an independent variable by both

methods. In terms of imperfections accuracy estimation, both proposed algorithms, TALS-STI and HOSVD-STI, show the same performance in the considered scenario. Note that the proposed TALS-STI and HOSVD-STI algorithms outperform the method in [24], even when an ideal non-impaired RIS is assumed. However, the gains achieved by our methods become more evident in the challenging scenario where the number of impaired elements at the RIS increases. In this case, the method of [24] is sensitive to  $R_B$ . Thus, if the number of impaired RIS elements changes, the method of [24] does not show a stable/predictable performance. This leads to the need for CE correction and retransmissions. In contrast, our proposed methods are quite robust to  $R_B$  variation, simplifying the system design.

## VI. CONCLUSION

We have proposed different efficient tensor-based algorithms for CE in RIS-assisted MIMO systems, in which the RIS elements are affected by real-world imperfections. We resort to the multidimensional structure of the received signal to solve these non-idealized CE problems by means of trilinear and quadrilinear PARAFAC models. The proposed TALS-LTI algorithm solves the problem when static imperfections are assumed. As a generalization, we have formulated the TALS-STI and HOSVD-STI algorithms for the more challenging scenario in which the behavior of the RIS imperfections is non-static with respect to channel coherence time. The TALS-LTI and TALS-STI algorithms are iterative solutions that relax the system design requirements, operating under more flexible choices for the training parameters. In contrast, the HOSVD-STI algorithm is a closed-form solution having a lower computational complexity compared to the competing ALS-based solutions while enjoying parallel processing. Numerical results illustrate the remarkable performance of the proposed tensor-based algorithms for different kinds of imperfections, channel models, and system configurations. The TALS-STI and HOSVD-STI algorithms present similar CE performances. However, the TALS-STI is preferable for the imperfections detection in the low SNR regime and when more flexible choices for training parameters is required, while the HOSVD-STI is preferred when low processing delay is desired.

## REFERENCES

- [1] G. Forecast, "Cisco visual networking index: global mobile data traffic forecast update, 2017–2022," *Update*, vol. 2017, p. 2022, 2019.
- [2] ITU, "IMT traffic estimates for the years 2020 to 2030," ITU-R M, TR 2370-0, Jan. 2015, V.15.0.0.
- [3] S. Zhang, Q. Wu, S. Xu, and G. Y. Li, "Fundamental green tradeoffs: Progresses, challenges, and impacts on 5G networks," *IEEE Commun. Surveys Tuts.*, vol. 19, no. 1, pp. 33–56, Feb. 2016.
- [4] C. Huang, A. Zappone, G. C. Alexandropoulos, M. Debbah, and C. Yuen, "Reconfigurable intelligent surfaces for energy efficiency in wireless communication," *IEEE Trans. Wireless Commun.*, vol. 18, no. 8, pp. 4157–4170, Aug. 2019.
- [5] B. Yang, X. Cao, C. Huang, C. Yuen, M. Di Renzo, Y. L. Guan, D. Niyato, L. Qian, and M. Debbah, "Federated spectrum learning for reconfigurable intelligent surfaces-aided wireless edge networks," *IEEE Trans. Wireless Commun.*, vol. 21, no. 11, pp. 9610–9626, Nov. 2022.
- [6] H. Guo, C. Madapatha, B. Makki, B. Dortschy, L. Bao, M. Åström, and T. Svensson, "A comparison between network-controlled repeaters and reconfigurable intelligent surfaces," 2022.

- [7] E. Basar, M. Di Renzo, J. De Rosny, M. Debbah, M.-S. Alouini, and R. Zhang, "Wireless communications through reconfigurable intelligent surfaces," *IEEE Access*, vol. 7, pp. 116 753–116 773, Jun. 2019.
- [8] Y. Liu, X. Liu, X. Mu, T. Hou, J. Xu, M. Di Renzo, and N. Al-Dhahir, "Reconfigurable intelligent surfaces: Principles and opportunities," *IEEE Commun. Surveys Tuts.*, vol. 23, no. 3, pp. 1546–1577, May 2021.
- [9] Q. Wu and R. Zhang, "Towards smart and reconfigurable environment: Intelligent reflecting surface aided wireless network," *IEEE Communications Magazine*, vol. 58, no. 1, pp. 106–112, Nov. 2019.
- [10] H. Guo, B. Makki, M. Åström, M.-S. Alouini, and T. Svensson, "Dynamic blockage pre-avoidance using reconfigurable intelligent surfaces," 2022. [Online]. Available: <https://arxiv.org/abs/2201.06659>
- [11] 3GPP, "RWS-210300 NR repeaters and reconfigurable intelligent surface," in *3GPP TSG RAN Rel-18 workshop*. Electronic Meeting, June 28 - July 2, 2021.
- [12] R. A. Tasci, F. Kilinc, E. Basar, and G. C. Alexandropoulos, "A new RIS architecture with a single power amplifier: Energy efficiency and error performance analysis," *IEEE Access*, vol. 10, pp. 44 804–44 815, Apr. 2022.
- [13] A. Zappone, M. Di Renzo, F. Shams, X. Qian, and M. Debbah, "Overhead-aware design of reconfigurable intelligent surfaces in smart radio environments," *IEEE Trans. Wireless Commun.*, vol. 20, no. 1, pp. 126–141, Jan. 2021.
- [14] Y. Chen, Y. Wang, Z. Wang, and P. Zhang, "Robust beamforming for active reconfigurable intelligent omni-surface in vehicular communications," *IEEE J. Sel. Areas Commun.*, pp. 1–1, 2022.
- [15] D. Mishra and H. Johansson, "Channel estimation and low-complexity beamforming design for passive intelligent surface assisted MISO wireless energy transfer," in *Proc. ICASSP "2019"*, Brighton, UK, Apr.
- [16] A. Taha, M. Alrabeiah, and A. Alkhatieb, "Enabling large intelligent surfaces with compressive sensing and deep learning," *IEEE Access*, vol. 9, pp. 44 304–44 321, Mar. 2021.
- [17] Y. Guo, P. Sun, Z. Yuan, C. Huang, Q. Guo, Z. Wang, and C. Yuen, "Efficient channel estimation for RIS-aided MIMO communications with unitary approximate message passing," *IEEE Trans. Wireless Commun.*, vol. 22, no. 2, pp. 1403–1416, Feb. 2023.
- [18] L. Wei, C. Huang, Q. Guo, Z. Yang, Z. Zhang, G. C. Alexandropoulos, M. Debbah, and C. Yuen, "Joint channel estimation and signal recovery for RIS-empowered multiuser communications," *IEEE Trans. Commun.*, vol. 70, no. 7, pp. 4640–4655, Jul. 2022.
- [19] B. Li, Z. Zhang, Z. Hu, and Y. Chen, "Joint array diagnosis and channel estimation for RIS-aided mmwave MIMO system," *IEEE Access*, vol. 8, pp. 193 992–194 006, Oct. 2020.
- [20] B. Li, Z. Zhang, and Z. Hu, "Channel estimation for reconfigurable intelligent surface-assisted multiuser mmwave MIMO system in the presence of array blockage," *Transactions on Emerging Telecommunications Technologies*, vol. 32, no. 11, p. e4322, Jun. 2021.
- [21] R. Sun, W. Wang, L. Chen, G. Wei, and W. Zhang, "Diagnosis of intelligent reflecting surface in millimeter-wave communication systems," *IEEE Tran. Wireless Commun.*, vol. 21, no. 6, pp. 3921–3934, 2022.
- [22] P. R. B. Gomes, G. T. de Araújo, B. Sokal, A. L. F. de Almeida, B. Makki, and G. Fodor, "Tensor-based channel estimation for RIS-assisted communications with non-ideal phase shift responses," in *Workshop on Commun. Networks and Power Syst. (WCNPS)*, 2022, pp. 1–6.
- [23] X. Qian, M. Di Renzo, J. Liu, A. Kammoun, and M.-S. Alouini, "Beamforming through reconfigurable intelligent surfaces in single-user MIMO systems: SNR distribution and scaling laws in the presence of channel fading and phase noise," *IEEE Wireless Commun. Lett.*, vol. 10, no. 1, pp. 77–81, Sep. 2021.
- [24] G. T. de Araújo, A. L. F. de Almeida, and R. Boyer, "Channel estimation for intelligent reflecting surface assisted MIMO systems: A tensor modeling approach," *IEEE J. Sel. Topics Signal Process.*, vol. 15, no. 3, pp. 789–802, Feb. 2021.
- [25] M.-A. Badiu and J. P. Coon, "Communication through a large reflecting surface with phase errors," *IEEE Wireless Commun. Lett.*, vol. 9, no. 2, pp. 184–188, Feb. 2020.
- [26] S. Zhou, W. Xu, K. Wang, M. Di Renzo, and M.-S. Alouini, "Spectral and energy efficiency of IRS-assisted MISO communication with hardware impairments," *IEEE wireless commun. lett.*, vol. 9, no. 9, pp. 1366–1369, Sep. 2020.
- [27] K. Zhi, C. Pan, H. Ren, and K. Wang, "Uplink achievable rate of intelligent reflecting surface-aided millimeter-wave communications with low-resolution ADC and phase noise," *IEEE Wireless Commun. Lett.*, vol. 10, no. 3, pp. 654–658, Mar. 2021.
- [28] R. Sun, W. Wang, L. Chen, G. Wei, and W. Zhang, "Diagnosis of intelligent reflecting surface in millimeter-wave communication systems," *IEEE Trans. Wireless Commun.*, vol. 21, no. 6, pp. 3921–3934, Jun. 2022.
- [29] J. Wang, S. Gong, Q. Wu, and S. Ma, "RIS-aided MIMO systems with hardware impairments: Robust beamforming design and analysis," *IEEE Trans. Wireless Commun.*, pp. 1–1, 2023.
- [30] N. Sidiropoulos, G. Giannakis, and R. Bro, "Blind PARAFAC receivers for DS-CDMA systems," *IEEE Trans. Signal Process.*, vol. 48, no. 3, pp. 810–823, Mar. 2000.
- [31] H. Chen, F. Ahmad, S. Vorobyov, and F. Porikli, "Tensor decompositions in wireless communications and MIMO radar," *IEEE J.Sel. Topics in Signal Process.*, vol. 15, no. 3, pp. 438–453, Feb. 2021.
- [32] N. D. Sidiropoulos, L. De Lathauwer, X. Fu, K. Huang, E. E. Papalexakis, and C. Faloutsos, "Tensor decomposition for signal processing and machine learning," *IEEE Trans. Signal Process.*, vol. 65, no. 13, pp. 3551–3582, Feb. 2017.
- [33] L. Wei, C. Huang, G. C. Alexandropoulos, C. Yuen, Z. Zhang, and M. Debbah, "Channel estimation for RIS-empowered multi-user MISO wireless communications," *IEEE Trans. Commun.*, vol. 69, no. 6, pp. 4144–4157, 2021.
- [34] G. T. de Araújo, P. R. B. Gomes, A. L. F. de Almeida, G. Fodor, and B. Makki, "Semi-blind joint channel and symbol estimation in IRS-assisted multiuser MIMO networks," *IEEE Wireless Commun. Lett.*, vol. 11, no. 7, pp. 1553–1557, Jun. 2022.
- [35] T. G. Kolda and B. W. Bader, "Tensor decompositions and applications," *SIAM review*, vol. 51, no. 3, pp. 455–500, Aug. 2009.
- [36] L. De Lathauwer, B. De Moor, and J. Vandewalle, "A multilinear singular value decomposition," *SIAM Journal on Matrix Analysis and Applications*, vol. 21, no. 4, pp. 1253–1278, Apr. 2000.
- [37] S. Abeywickrama, R. Zhang, Q. Wu, and C. Yuen, "Intelligent reflecting surface: Practical phase shift model and beamforming optimization," *IEEE Trans. Commun.*, vol. 68, no. 9, pp. 5849–5863, Sep. 2020.
- [38] Z. Yigit, E. Basar, and I. Altunbas, "Low complexity adaptation for reconfigurable intelligent surface-based MIMO systems," *IEEE Commun. Lett.*, vol. 24, no. 12, pp. 2946–2950, Dec. 2020.
- [39] B. Sokal, P. R. B. Gomes, A. L. F. de Almeida, B. Makki, and G. Fodor, "IRS phase-shift feedback overhead-aware model based on rank-one tensor approximation," in *Proc. IEEE GLOBECOM 2022*, Dec. 2022, pp. 3911–3916.
- [40] —, "Reducing the control overhead of intelligent reconfigurable surfaces via a tensor-based low-rank factorization approach," *IEEE Trans. Wireless Commun.*, pp. 1–1, 2023.
- [41] Q. Wu and R. Zhang, "Beamforming optimization for wireless network aided by intelligent reflecting surface with discrete phase shifts," *IEEE Trans. Commun.*, vol. 68, no. 3, pp. 1838–1851, Mar. 2020.
- [42] H. Guo, Y.-C. Liang, J. Chen, and E. G. Larsson, "Weighted sum-rate maximization for intelligent reflecting surface enhanced wireless networks," in *Proc. IEEE GLOBECOM 2019*, Dec. 2019, pp. 1–6.
- [43] R. Bro, "Multi-way analysis in the food industry models, algorithms & applications," 1998.
- [44] X.-F. Gong and Q.-H. Lin, "Spatially constrained parallel factor analysis for semi-blind beamforming," in *Proc. International Conference on Natural Computation*, vol. 1. IEEE, 2011, pp. 416–420.
- [45] Z. Wang, C. Cai, F. Wen, and D. Huang, "A quadrilinear decomposition method for direction estimation in bistatic MIMO radar," *IEEE Access*, vol. 6, pp. 13 766–13 772, Mar. 2018.
- [46] T. L. Jensen and E. De Carvalho, "An optimal channel estimation scheme for intelligent reflecting surfaces based on a minimum variance unbiased estimator," in *proc. ICASSP "2020"*, Barcelona, Spain, May.
- [47] Z.-Q. He and X. Yuan, "Cascaded channel estimation for large intelligent metasurface assisted massive MIMO," *IEEE Wireless Commun. Lett.*, vol. 9, no. 2, pp. 210–214, Feb. 2019.
- [48] B. Sokal, P. R. B. Gomes, A. L. F. de Almeida, and M. Haardt, "Tensor-based receiver for joint channel, data, and phase-noise estimation in MIMO-OFDM systems," *IEEE J. Sel. Topics Signal Process.*, vol. 15, no. 3, pp. 803–815, Apr. 2021.
- [49] G. Zhou, C. Pan, H. Ren, P. Popovski, and A. L. Swindlehurst, "Channel estimation for RIS-aided multiuser millimeter-wave systems," *IEEE Trans. Signal Process.*, vol. 70, pp. 1478–1492, 2022.